Journal of Energy Storage 178 (2026) 123341

Contents lists available at ScienceDirect

Journal of Energy Storage

journal homepage: www.elsevier.com/locate/est

Research papers

Cycle-wise detrending method for strain-based aging characterization and feature development of batteries: Case study of 18650 NMC Li-ion cells

Malichi Flemming II [a], George Anthony [a], Ryan L. Limbaugh [a], Austin R.J. Downey [a,b,*]

[a] Department of Mechanical Engineering, University of South Carolina, Columbia, 29208, SC, USA
[b] Department of Civil Engineering, University of South Carolina, Columbia, 29208, SC, USA

ARTICLE INFO

Dataset link: Dataset-1 (Original data)

Keywords:
Lithium ion
State-of-health
Battery degradation
Mechanical stress
Strain gauge
Strain decomposition
Intercalation
Solid electrolyte interphase
Lithium plating
Residual strain

ABSTRACT

Accurate assessment of lithium-ion battery state of health (SOH) is essential for ensuring their safe and reliable operation, particularly under abnormal conditions such as overcharging. This study investigates the use of strain measurements to evaluate the SOH of a 3000 mAh Samsung 30Q cell subjected to standard cycling and an overcharge event introduced midway through its expected lifetime. Continuous strain gauge-based monitoring revealed distinct changes in residual deformation following overcharge, indicating irreversible structural modification. A strain-decomposition framework was developed to separate cyclic deformation into offset, slope, and residual components. The offset captured irreversible baseline shifts associated with cumulative degradation, while the slope reflected reversible, SOC-dependent expansion and contraction. The residual component isolated nonlinear intercalation-driven deformation, providing a sensitive indicator of evolving internal electrochemical conditions. Feature-based analysis of the residual strain incorporated distribution-shape features, in addition to both time-domain and frequency-domain metrics. Maximum strain and root mean square frequency (RMSF) exhibited the strongest cross-cell consistency, with average Spearman correlations exceeding 95% and median absolute differences below 4%. Principal component analysis further revealed distinct mechanical signatures between charging and discharging. Charging PC1 was dominated by waveform-shape descriptors such as skewness, shape factor, and crest factor, whereas discharging PC1 was governed primarily by strain-magnitude features, including RMSF, maximum strain, and mean strain, aligning more with feature correlation results. These complementary modes captured approximately 99% of the total variance across the first five charging and discharging components. Post-overcharge analysis displayed clear increases in residual strain and changes in slope, consistent with irreversible structural damage and aligned with observed reductions in electrical performance. This work establishes a foundation for integrating mechanical strain diagnostics into future battery management systems.

1. Introduction

Lithium-ion batteries are integral to modern energy storage applications [1]. Electric vehicles, smart grid storage, and consumer electronics are just a few examples where lithium-ion batteries are becoming increasingly prevalent. One key metric for assessing battery performance over time is state-of-health (SOH), which indicates the battery's ability to charge and discharge throughout its lifespan in comparison to its initial condition [2,3]. As the usage of lithium-ion batteries expands, ensuring the safety, reliability, and longevity of these cells has become increasingly critical [4,5], requiring more accurate SOH monitoring and prediction.

Common battery models such as integer-order equivalent circuit models (IOECMs) are simple and computationally efficient, but cannot capture hidden internal states [6,7]. In contrast, fractional-order equivalent circuit models (FOECMs) facilitate more sophisticated feature extraction at the expense of increased computational demand [8,9]. While offering highly accurate representations of underlying battery physics, electrochemical models are sensitive to age-induced degradation and parameter variations. Data-driven approaches, such as neural networks, require extensive training and large datasets and may exhibit poor generalization when exposed to conditions outside the training domain [10]. Moreover, training models for accurate SOH estimation is challenging due to complex degradation mechanisms influenced by temperature, charge/discharge cycling, and diverse operational conditions [11].

* Corresponding author at: Department of Mechanical Engineering, University of South Carolina, Columbia, 29208, SC, USA.
E-mail address: austindowney@sc.edu (A.R.J. Downey).

https://doi.org/10.1016/j.est.2026.123341
Received 31 January 2026; Received in revised form 25 April 2026; Accepted 27 June 2026
Available online 17 July 2026

Traditional methods for assessing lithium-ion battery cell degradation throughout charge–discharge cycling, such as impedance spectroscopy and capacity fade analysis, often require intrusive measurements or fail to provide real-time insights. Measurable signals, particularly voltage, current, and temperature, offer limited precision as they can only observe key internal battery states indirectly. More recent methods have also been established, each presenting distinct benefits. Strain gauges and piezoelectric films are recognized for their cost-effectiveness and scalability in facilitating real-time monitoring [12,13]. In contrast, fiber Bragg grating (FBG) sensors offer enhanced sensitivity through the utilization of optical signals [14]. Digital image correlation (DIC) provides a non-contact means for surface deformation tracking [15], while advanced techniques such as X-ray diffraction (XRD) and neutron scattering enable the characterization of internal lattice strain [16,17]. Additionally, finite element modeling (FEM) serves as a valuable computational tool, simulating strain behavior under diverse conditions to inform design and safety optimization [18].

Of these newer approaches, strain sensing provides a direct mechanical signature of the electrochemical reactions and degradation processes occurring within the cell. This includes the dynamic volumetric changes that occur in electrode materials during lithiation and delithiation, such as expansion, contraction, and phase transitions in graphite [14]. Incorporating in-situ monitoring of battery deformations can capture reversible strain dynamics over charge/discharge cycles as well as irreversible growth associated with aging and SEI formation [19,20]. As a result, strain sensing has emerged as a promising complementary modality for battery state estimation [21,22], enabling data-driven mapping from mechanical signatures to SOC and SOH when combined with multi-sensor integration and machine learning models. This methodology not only improves SOC estimation performance, but also provides early detection of cell imbalance, mechanical degradation, and capacity fade, thereby aiding the development of advanced BMS algorithms for safety management, fault detection, and lifetime optimization [23]. The exploitation of mechanical–electrochemical coupling thus opens a new avenue for precise, non-invasive battery state estimation, bridging electrochemical modeling with real-time sensor data to achieve intelligent and resilient battery operation under diverse cycling and environmental conditions [24].

Li et al. [25] highlight the difficulty of joint SOC and SOH estimating due to their intrinsic coupling. Their work demonstrates that strain measurements vary with SOH even when SOC remains unchanged, enabling improved separation of the two states. The authors also emphasize that strain sensing supports early SOH detection, as mechanical deformation associated with aging appears before electrical indicators exhibit changes. Despite its promise, reliable extraction of SOH-relevant information from strain signals remains challenging due to nonlinear swelling and the dominance of cycling-induced deformation. To overcome these limitations, work focusing on isolating the strain component associated with electrochemical processes is required to enable reliable strain-based feature extraction and analysis.

In this work, we propose a novel cycle-wise detrending method and show how combining it with strain gauge measurements can provide unique diagnostic insight into cell health. The proposed decomposition separates strain into three distinct elements: the *offset*, representing permanent baseline shifts due to irreversible changes such as solid electrolyte interphase (SEI) growth and lithium plating [26]; the *slope*, corresponding to reversible expansion and contraction during intercalation and deintercalation; and the *residual*, capturing nonlinearities associated with lithium staging transitions and other fine-structure phenomena. By applying this framework across repeated cycles, we examine how each component evolves with aging [27] and under abnormal conditions, including an overcharge event, and assess its potential as a sensitive diagnostic metric for SOH monitoring. The contributions of this work are threefold. First, we demonstrate that strain gauges mounted directly on cylindrical 18650 lithium-ion cells provide a practical and reliable means of collecting and reporting novel strain data during aging. Second, we present a method for decomposing strain measurements into distinct components that directly relate to reversible and irreversible cell deformation, thereby connecting mechanical response with electrochemical mechanisms. Third, we perform a statistical analysis of four categories of features extracted from the decomposed strain components demonstrating that waveform-shape features dominate charging and amplitude features dominate discharging.

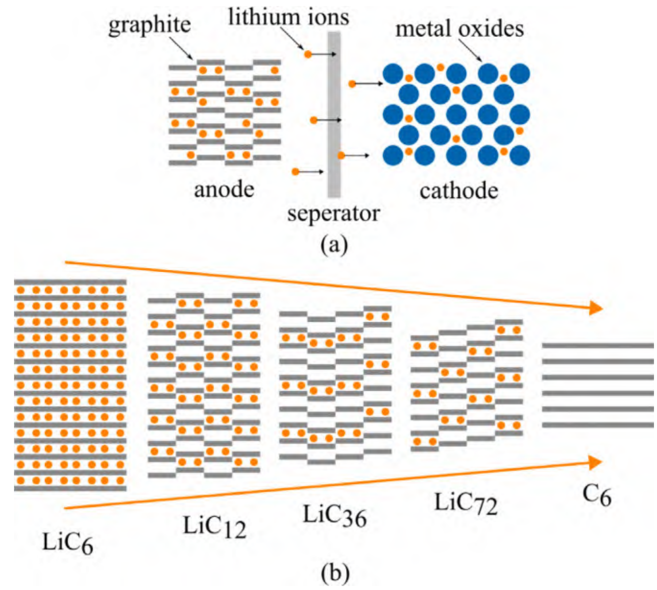

Fig. 1. Lithium ion migration between anode and cathode.

2. Relevant background

This section provides background on expansion and contraction of lithium cells during cycling. It subsequently details how these mechanical changes contribute to capacity loss by facilitating solid electrolyte interphase growth and lithium plating.

2.1. Reversible and irreversible strain

The intercalation of lithium ions between the anode and cathode, represented in Fig. 1, is the primary driver of reversible strain in lithium-ion batteries [28]. During charging, lithium ions migrate from the cathode through the separator in the electrolyte and embed themselves between the graphene layers of the graphite anode [29]. This process causes the anode to swell as the graphite lattice expands to accommodate the inserted lithium ions. Conversely, during discharge, the lithium ions deintercalate from the graphite anode and return to the cathode, resulting in contraction of the anode structure. This cyclic expansion and contraction of the graphite lattice is the fundamental reversible mechanical response of the cell, and it can be measured externally as hoop strain on cylindrical cells.

2.2. Solid electrolyte interphase

The formation of SEI constitutes a protective layer developed from the decomposition of electrolyte that occurs as it interacts with the anode material during the initial charging phase of a new battery cell [30,31]. This pivotal process enables the flow of lithium ions to and from the anode while simultaneously obstructing internal electron movement. Upon the establishment of this delicate passive layer, the

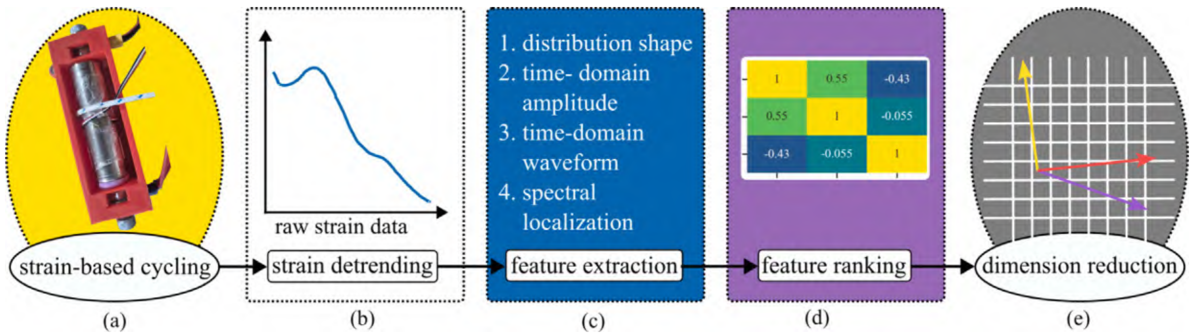

Fig. 2. Overview of the cyclewise detrending framework illustrating: a. data processing, b. decomposed strain, c. feature extraction, d. feature ranking, and e. correlation analysis.

chemical reaction ceases, effectively halting further electrolyte decomposition [32]. Notably, mechanical stress induced by the anode's expansion and contraction during cycling can result in the cracking or fracturing of the SEI layer, which in turn stimulates additional SEI accretion. This process culminates in the accumulation of an irreversibly thicker layer over time, which diminishes the availability of electrolyte necessary for lithium ion migration [12]. Wang et al. [30] have modeled the reversible and irreversible expansion processes, elucidating their implications for cell performance over time.

2.3. Lithium plating

Lithium plating is another contributor to irreversible cell expansion. Lithium plating transpires when the migration of lithium ions is impeded due to factors such as SEI growth, elevated charge/discharge rates, overcharging, overvoltage conditions, or charging at extremely low temperatures [33]. When lithium ions encounter difficulty during migration, they may crystallize into lithium metal deposits on the anode. This accumulation of lithium plating progressively restricts lithium ion flow and poses the risk of dendrite formation, characterized by needle-like projections of lithium metal that can breach the cell layers, leading to further degradation or potential short-circuiting of the cell. Moreover, the reduction of free lithium ions results in a diminished charge capacity of the cell, which corresponds to a lower SOH.

The measurement of mechanical strain has emerged as a diagnostic tool for identifying abnormal conditions within lithium-ion cells. Instances of overcharging and cell abuse can generate significant variations in internal pressure, which yield detectable measurements within the cell. Kirchev et al. [34] have demonstrated that, in similar 18650 cells, it is feasible to detect the onset of cell over-swell almost immediately following an overcharge event. Additionally, research conducted by Anthony et al. reveals that strain measurement can serve as a reliable indicator of failures in current interrupt devices (CIDs) in 18650 cells, supported by strain data [15].

3. Methodology

This section outlines the experimental setup, data acquisition and processing pipeline, and evaluation procedures used to validate performance and ensure reproducibility. Fig. 2 is a visual outline displaying the step-by-step method used in this paper.

First, a strain gauge and thermocouple are adhered to the cell and placed in a holder that connects the cells to a battery cycler module shown in Fig. 3. Once the cycling data is stored and processed, the raw strain data is detrended to the residual strain for each cycle. Features are extracted from the residual strain data, which are categorized by distribution shape, time-domain amplitude, time-domain waveform, or spectral localization. The extracted features are ranked using the Spearman correlation method and dimensionally reduced using principal component analysis (PCA).

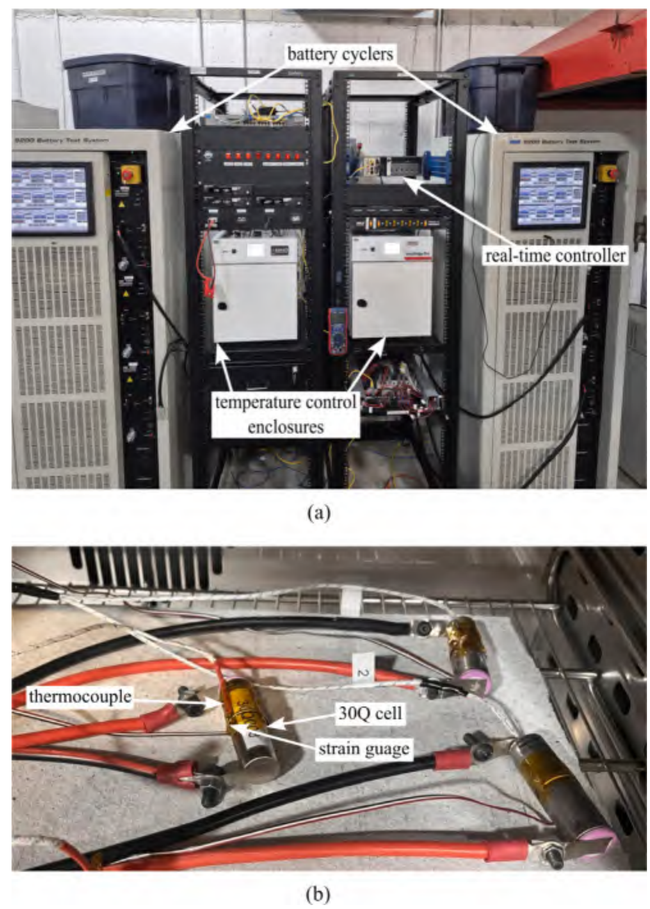

Fig. 3. Images presenting: (a) the battery lab experimental setup, and (b) three 18 650 cells with strain gauges and thermocouples inside a temperature control enclosure.

3.1. Experimental testing

A set of three lithium-ion cells from the same order batch (Samsung 30Q), with a nominal capacity of 3000 mAh, were subjected to a testing regimen utilizing a constant current–constant voltage (CCCV) charging method, followed by a constant current (CC) discharge at a rate of 1C. Each test cycle incorporated a one-hour rest period between the charging and discharging phases. Current and voltage were supplied to the cells and measured via three 12 kW bi-directional DC modules (NHR4912, NH Research) housed in a battery test system chassis (NHR9200, NH Research). The hoop strain and temperature of the cells were measured individually using surface-mounted 350 ohm strain gauges (MMF404146, Micro-Measurements) and K-type thermocouples, respectively. The strain gauges were bonded to the cells with an rapid-curing adhesive specifically formulated for strain-gauge bonding (M-Bond 200, Micro-Measurements), and is compatible with all Micro-Measurements strain gauges [35,36]. Great care was taken to ensure a very thin, uniform adhesive layer was applied to produce a thin localized layer maximizing strain-transfer accuracy. The cell is lightly sanded for better adhesion and the strain gauge is mounted circumferentially at the center of the cell to measure hoop strain. The data acquisition system consisted of a laptop computer (ThinkPad T470s, Lenovo) and a compactDAQ chassis (CDAQ-9189, National Instruments) housing a 4-channel, 24-bit thermocouple measurement module (NI-9212, National Instruments) and a 8-channel, 24-bit quarter-bridge strain input module (NI-9236, National Instruments). The battery cycling process continued until the cells' capacities were observed for 450 cycles, which is approximately 80% of their initial capacity. The capacity for each cycle was quantified through the integration of current over time via Coulomb counting, while the cells' nominal state of health (SOH) was computed as a percentage of the rated capacity. All experimental date from these tests is provided as "Dataset-1" through a more comprehensive public repository [37] and provided as supplemental data with this publication.

3.2. Strain decomposition

To derive insights regarding the mechanical behavior from the strain measurements, the strain signals for each cycle were decomposed into three distinct components: offset, slope, and residual. The offset, characterized by the initial strain value at the commencement of discharge, was systematically subtracted from all subsequent strain data points. The slope, established as the linear trend between the initial and final strain values, was also removed.

We define the lithium stoichiometry $\theta(t)$ as the fractional lithium content of the graphite anode ($0 \leq \theta \leq 1$). Under constant-current operation,

$$I = \frac{dQ}{dt} = \text{const}, \tag{1}$$

so the passed charge evolves linearly,

$$Q(t) = It + Q_0. \tag{2}$$

Because lithium intercalation proceeds at a constant molar flux,

$$\theta(t) = \theta_0 + kt, \tag{3}$$

therefore

$$\theta - \theta_0 = \alpha(Q - Q_0). \tag{4}$$

The measured strain is modeled as

$$\varepsilon(Q) = f\left(\theta(Q)\right) + \varepsilon_{\text{mech}}(Q), \tag{5}$$

where $f(\theta)$ is the reversible lithiation-induced swelling and $\varepsilon_{\text{mech}}(Q)$ captures background mechanical effects. Since f is smooth, a Taylor expansion about θ_0 gives

$$f(\theta) = f(\theta_0) + f'(\theta_0)(\theta - \theta_0) + \tfrac{1}{2} f''(\theta_0)(\theta - \theta_0)^2 + \mathcal{O}\left((\theta - \theta_0)^3\right). \tag{6}$$

Substituting $\theta - \theta_0 = \alpha(Q - Q_0)$ yields

$$\varepsilon(Q) \approx f(\theta_0) + B(Q - Q_0) + C(Q - Q_0)^2 + \varepsilon_{\text{mech}}(Q), \tag{7}$$

with

$$B = f'(\theta_0)\alpha, \qquad C = \tfrac{1}{2} f''(\theta_0)\alpha^2. \tag{8}$$

We define the intra-cycle offset as the strain at the start of charge,

$$\varepsilon_{\text{off}} = \varepsilon(Q_0), \tag{9}$$

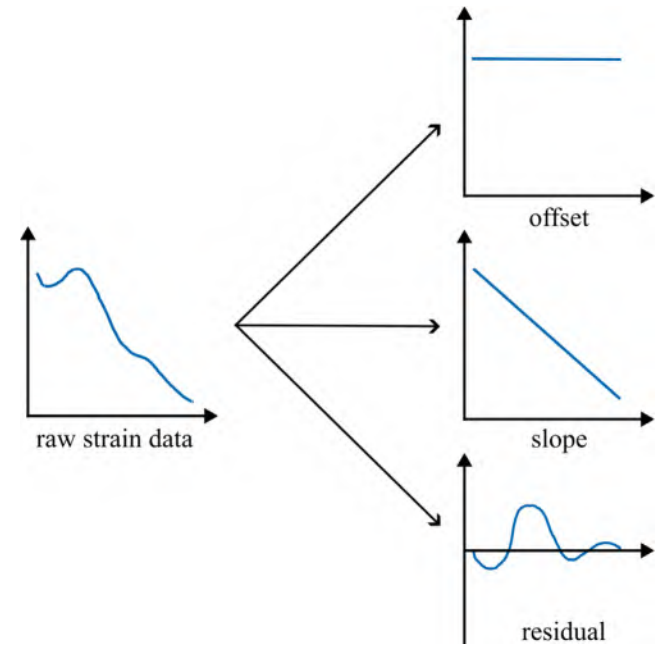

Fig. 4. Breakdown of strain decomposition methodology.

and subtract it to isolate the charge-dependent variation,

$$\tilde{\varepsilon}(Q) = \varepsilon(Q) - \varepsilon_{\text{off}}. \tag{10}$$

The offset–subtracted strain becomes

$$\tilde{\varepsilon}(Q) \approx B(Q - Q_0) + C(Q - Q_0)^2 + \varepsilon_{\text{mech,res}}(Q), \tag{11}$$

where $\varepsilon_{\text{mech,res}}(Q)$ collects higher-order and non-chemo-mechanical contributions. The extracted linear component is

$$\tilde{\varepsilon}_{\text{lin}}(Q) = B(Q - Q_0), \tag{12}$$

and the remaining nonlinear and degradative contributions are

$$\tilde{\varepsilon}_{\text{res}}(Q) = \tilde{\varepsilon}(Q) - \tilde{\varepsilon}_{\text{lin}}(Q). \tag{13}$$

The residual strain (Eq. (13)), which is essentially the signal that remained post-removal of both the offset (Eq. (9)) and slope (Eq. (12)), was employed for in-depth analytical investigation displayed in Fig. 4. A variety of time and frequency domain features were extracted from the residual strain signals across each cycle, aiming to explore their correlations with capacity degradation.

3.3. Preliminary data exploration

This section presents a basic and preliminary data exploration into the capacity vs. cycle data. Following the initial 100 cycles, the growth of SEI reaches a state of stabilization, permitting the strain response of the cell to establish a consistent pattern throughout the remainder of the testing period. This sustained response is characterized by a diminishing trend in hoop strain during the discharge phase; conversely, the charging process exhibits a parallel behavior, reflected in increasing strain levels. In Fig. 5, the strain data is delineated into offset, slope, and residual components, with the residual component capturing the nonlinear characteristics of the signal utilized for feature analysis.

The overall capacity degradation trajectory across approximately 450 cycles is shown in Fig. 6. This plot presents the measured capacity of three Samsung 30Q cells over their lifetime, with two prominent overcharge incidents marked during cycling. These overcharge events serve as natural perturbations within the dataset, producing accelerated degradation and providing a useful benchmark to compare changes

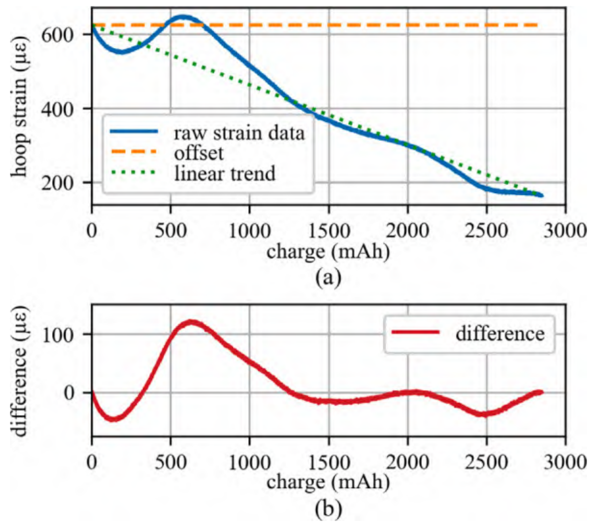

Fig. 5. Strain data characterization by partitioning into three distinct components: the offset, the linear trend, and the residual (difference).

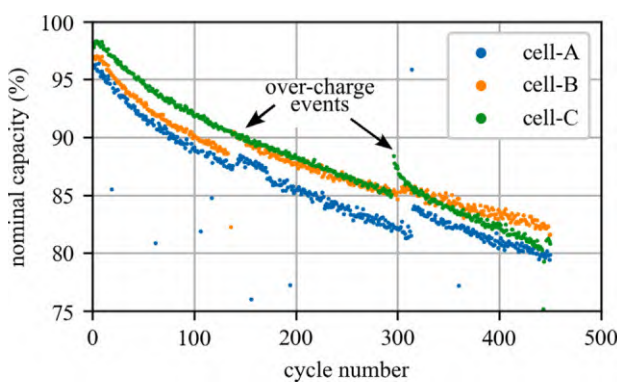

Fig. 6. Nominal capacity data for three 18 650 cells with over-charge event.

in both electrical and mechanical response. The capacity fade follows the typical declining trend toward end-of-life at approximately 80% SOH, but the step-changes induced by the overcharge highlight how abnormal cycling conditions can strongly alter the subsequent strain response.

Fig. 7(a) presents the charge data for Cell A at cycle 100. It shows strain, voltage, temperature, and current throughout the CCCV charge process. A key observation is the decoupled nature of the strain and temperature responses. During the CC portion of charging, strain increases steadily with lithium intercalation into the graphite anode, while the cell temperature also rises steadily. Entering the constant voltage (CV) region, the behavior diverges. Strain and temperature initially decreases as the current begins to drop. However, as the cell approaches full charge, strain increases once more while temperature continues to drop rapidly as the charging current decreases. This pattern indicates that strain is primarily linked to the staging of lithium intercalation rather than thermal effects, with distinct inflection points aligning with electrochemical transitions within the graphite lattice.

The discharge profile of the same cell at cycle 100 is shown in Fig. 7(b). Here, strain initially increases alongside a gradual rise in cell temperature, consistent with early-stage deintercalation. However, as the discharge proceeds further, the strain decreases toward its baseline level while the cell temperature remains elevated due to resistive heating. This again underscores that while thermal effects contribute to the measurement environment, the strain gauge predominantly reflects the reversible structural contraction of the graphite anode during lithium extraction.

To evaluate the robustness of the strain signal under varying operating conditions, Fig. 8 compares strain trends across multiple charge and discharge rates. While minor differences are observed at extreme rates, the overall strain curve maintains a consistent shape aligned with the state of charge. This indicates that the strain response is more closely tied to the intercalation state of the anode than to the rate of lithium-ion transport, making it a reliable proxy for internal electrochemical processes independent of applied current rate.

Finally, Fig. 9 highlights the interaction between strain and temperature under controlled thermal conditions. The cell was cycled at a 1C rate within a 10°C environment, with strain and temperature monitored simultaneously. The results show that although temperature fluctuations are present, the strain response retains a distinct trajectory correlated with the electrochemical state. Temperature variance exhibited slow thermal drift, whereas, the mechanical strain displayed a sharp curve indicative of deintercalation dynamics. This further supports the interpretation that strain can be isolated from thermal artifacts and used as an independent diagnostic signal of intercalation dynamics and aging.

3.4. Feature-based investigation

3.4.1. Distribution shape (non-Gaussianity)

Distribution shape (non-Gaussianity) captures both asymmetry and tail heaviness in the residual strain. It is sensitive to early regime changes and departures from Gaussian behavior, which often precede shifts in averages or variability.

- Skewness (more specifically, sample skewness) was calculated using the Fisher–Pearson standardized moment coefficient (also known as the adjusted Fisher–Pearson coefficient), defined as

$$g_1 = \frac{m_3}{m_2^{3/2}}, \tag{14}$$

where $m_3 = \frac{1}{n}\sum_{i=1}^{n}(x_i - \bar{x})^3$ is the third central moment, $m_2 = \frac{1}{n}\sum_{i=1}^{n}(x_i - \bar{x})^2$ is the second central moment (variance), n is the sample size, and $\bar{x}$ is the sample mean.

- Kurtosis (more specifically sample kurtosis) g_2 (excess kurtosis) is computed as

$$g_2 = \frac{n(n+1)}{(n-1)(n-2)(n-3)}\sum_{i=1}^{n}\left(\frac{x_i - \bar{x}}{s}\right)^4 - \frac{3(n-1)^2}{(n-2)(n-3)}, \tag{15}$$

where s is the sample standard deviation. The first term is a scaled and normalized fourth moment, and the second term subtracts the bias correction and 3 to yield excess kurtosis.

3.4.2. Time-domain amplitude statistics

Time-domain amplitude statistics summarize level and range over a cycle, providing a stable, low-cost readout of load severity and slow baseline drift in the strain response.

- Mean strain ($\varepsilon_{\text{mean}}$) is the average strain value, representing the midpoint of the strain cycle.
- Minimum strain (ε_{min}) is the lowest strain value experienced, typically the compressive peak.
- Maximum strain (ε_{max}) is the highest strain value experienced, typically the tensile peak during a loading cycle, and is expressed as

$$\varepsilon_{\text{mean}} = \frac{\varepsilon_{\text{max}} + \varepsilon_{\text{min}}}{2}. \tag{16}$$

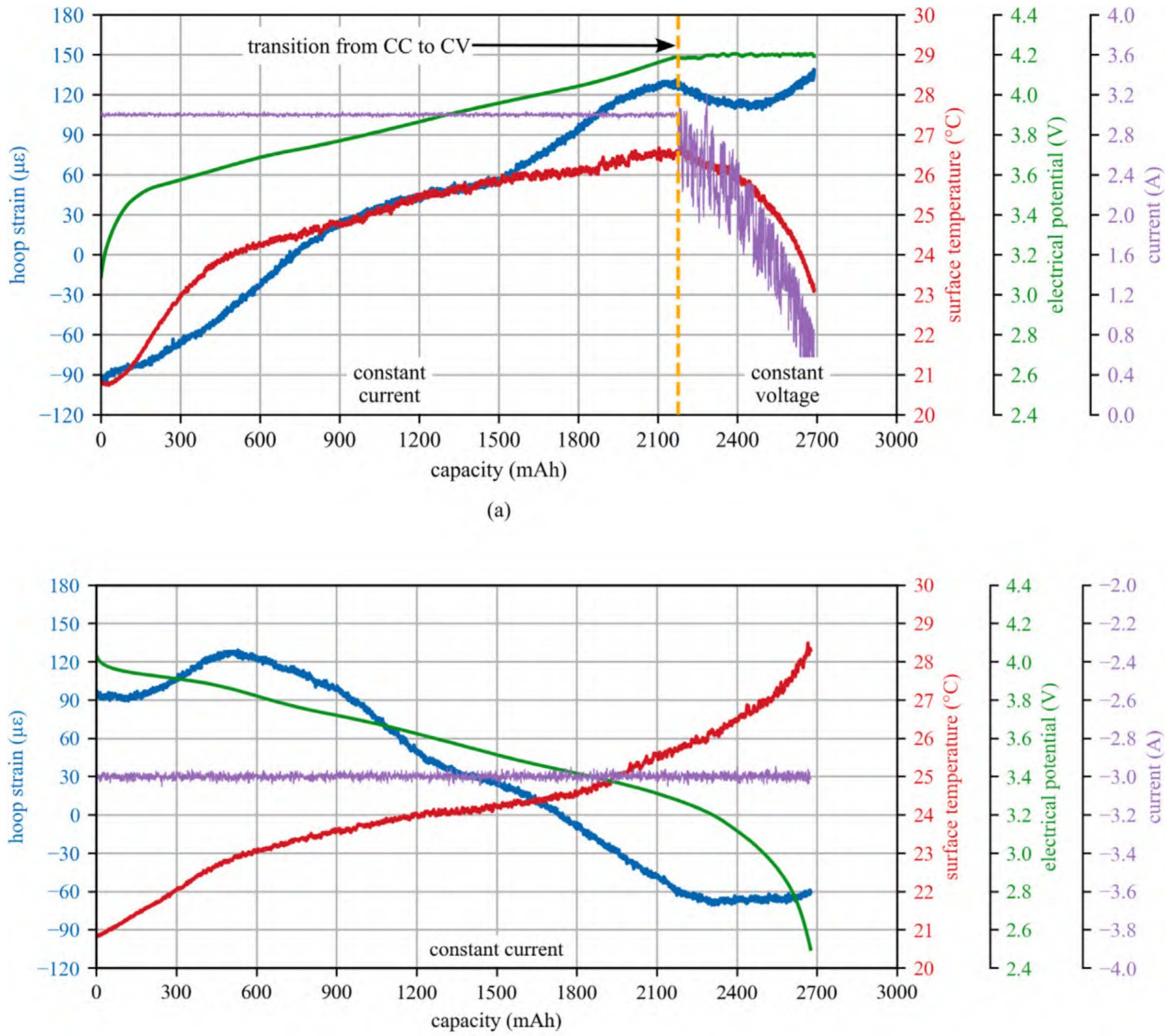

Fig. 7. Cycle 100 data for cell A collected: (a) during charge at 1C CCCV and (b) during discharge at 1C CC.

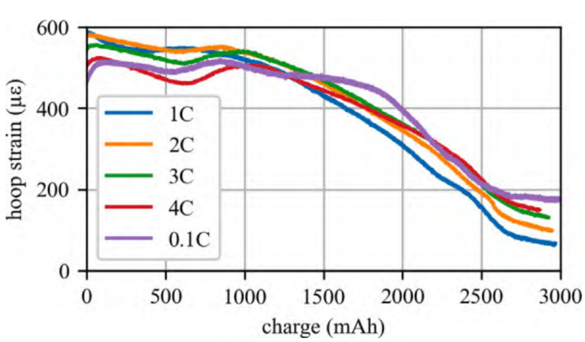

Fig. 8. Analysis of various strain trends across several discharge rates.

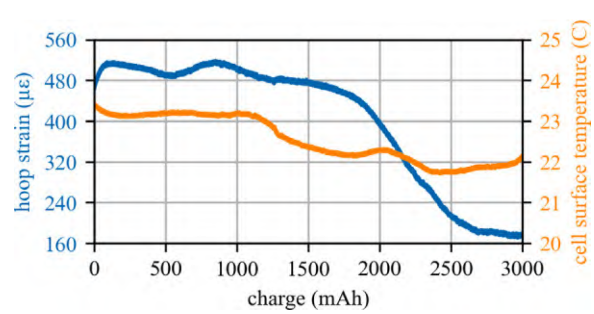

Fig. 9. Cell surface temperature and strain in 10 degree Celsius controlled environment cycled at a 1C rate.

3.4.3. Time-domain waveform ratios

Time-domain impulsiveness and shape ratios emphasize spike-like events and waveform form via peak-to-average relationships, highlighting short, high-energy transients that basic amplitude summaries may miss.

- Shape factor is the ratio of overall energy to average magnitude, capturing waveform form relative to its typical level. Computed as

$$\text{Shape} = \frac{\text{RMS}(x)}{\frac{1}{n}\sum_{i=1}^{n}|x_i|}. \tag{17}$$

Higher values indicate a more peaked waveform for the same average magnitude.

- Impulse is the ratio of the highest excursion to the average magnitude, emphasizing short, high-amplitude events. Computed as

$$\text{Impulse} = \frac{\max_i |x_i|}{\frac{1}{n}\sum_{i=1}^{n}|x_i|}. \tag{18}$$

Larger values indicate isolated spikes that can precede visible changes in simpler statistics.

- Crest Factor is widely used in vibration analysis and fault detection; the crest factor indicates the presence of sharp, high-energy spikes. It is defined as

$$\text{Crest Factor} = \frac{\text{Peak Value}}{\text{RMS}}. \tag{19}$$

An increase in crest factor often signals the development of faults even when total energy remains low.

3.4.4. Spectral localization

Spectral localization characterizes where strain energy concentrates in frequency, revealing resonance shifts and energy reallocation associated with protocol changes and evolving mechanical state.

- Root Mean Square Frequency (RMSF) provides a measure of the distribution of signal energy across frequency components. It is a weighted average frequency, useful in vibration and audio analysis.
- Frequency Center represents the central or resonant frequency around which a signal or filter is most active. It is defined as the midpoint between the lower cutoff frequency f_1 and the upper cutoff frequency f_2. Computed as

$$f_{\text{center}} = \frac{f_1 + f_2}{2}. \tag{20}$$

4. Results

This section presents and discusses the results from this work.

4.1. Detrended strain components

Figs. 10 and 11 summarize the cycle-wise offset and slope features computed separately for charge and discharge segments, revealing complementary aspects of baseline shift and intra-cycle trend. The offset feature in Figs. 10(a) and 11(a) tracks quasi-static drift in the residual strain (baseline expansion/contraction), while the slope feature in Figs. 10(b) and 11(b) captures dynamic evolution within a segment (rate-dependent accumulation). Full strain data plots were not included in the main paper for brevity, but can be found in Fig. 18 of Appendix.

Early cycles in Figs. 10 and 11 show tight clustering and near-zero slopes, indicating stable operation. With aging, both charge and discharge offsets diverge from zero and the slopes become increasingly non-zero, signaling progressive irreversibility. The offset plots are the initial points beginning the charge and discharge states per cycle, reflecting irreversible baseline shifts, and the slopes highlight the evolving reversible strain occurring during cycling as observed in Fig. 18. Notably, charge and discharge exhibit asymmetric behavior where charge offsets generally grow (positively or negatively) earlier and more monotonically, whereas discharge slopes are more sensitive to disturbances and protocol changes, producing detectable inflection points. Together, these features provide a low-cost, high-stability indicator set, and their divergence as cycling matures is consistent with the onset and progression of degradation.

Figs. 12 and 13 show the residual strain after cycle-wise detrending for charge (Fig. 12) and discharge (Fig. 13), plotted on matched axes for direct comparison. Early cycles exhibit minimal residual effects, indicating the initial health of new cells. With continued cycling, the residuals broaden and develop visible structure, signaling increasing non-stationarity and irreversible contributions. Both charge and discharge traces show a gradual increase in variance with generally smooth evolution. The outliers in both plots correspond to the overcharge events in Fig. 6.

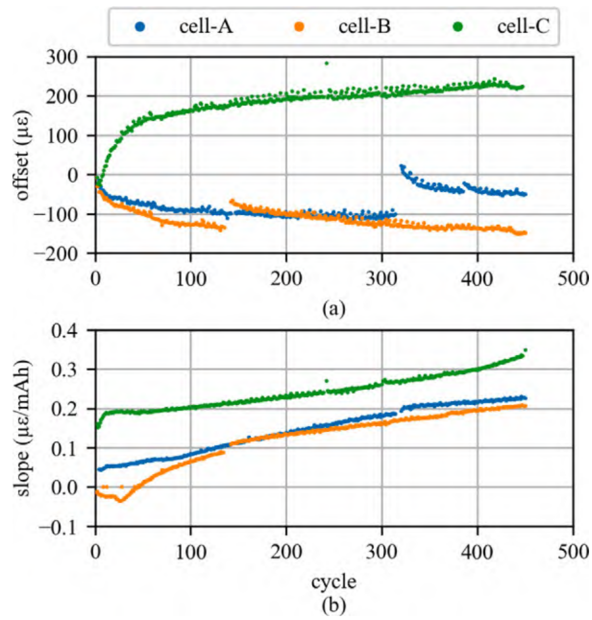

Fig. 10. Charging offset and slope data for cells A, B, and C.

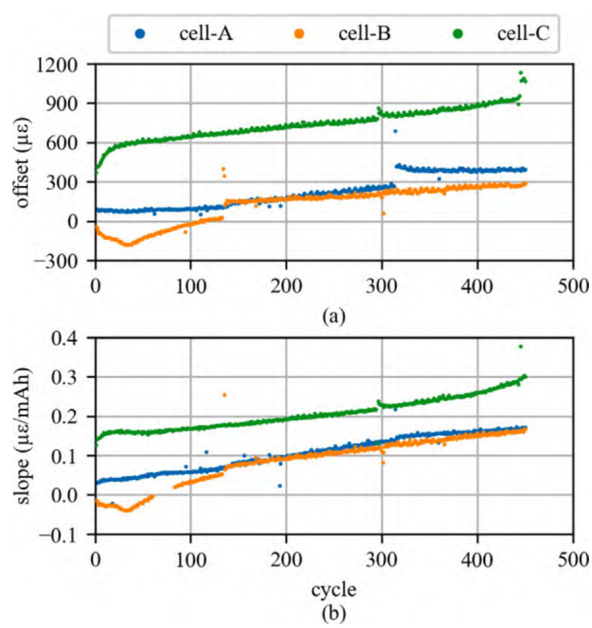

Fig. 11. Discharging offset and slope data for cells A, B, and C.

4.2. Strain feature analysis

Figs. 14 and 15 compile all extracted strain-based features across cycles using common axes for direct comparison, with Fig. 14 showing charge and Fig. 15 showing discharge. The panels reveal three consistent patterns. First, the distribution shape features (sub-figures (a) and

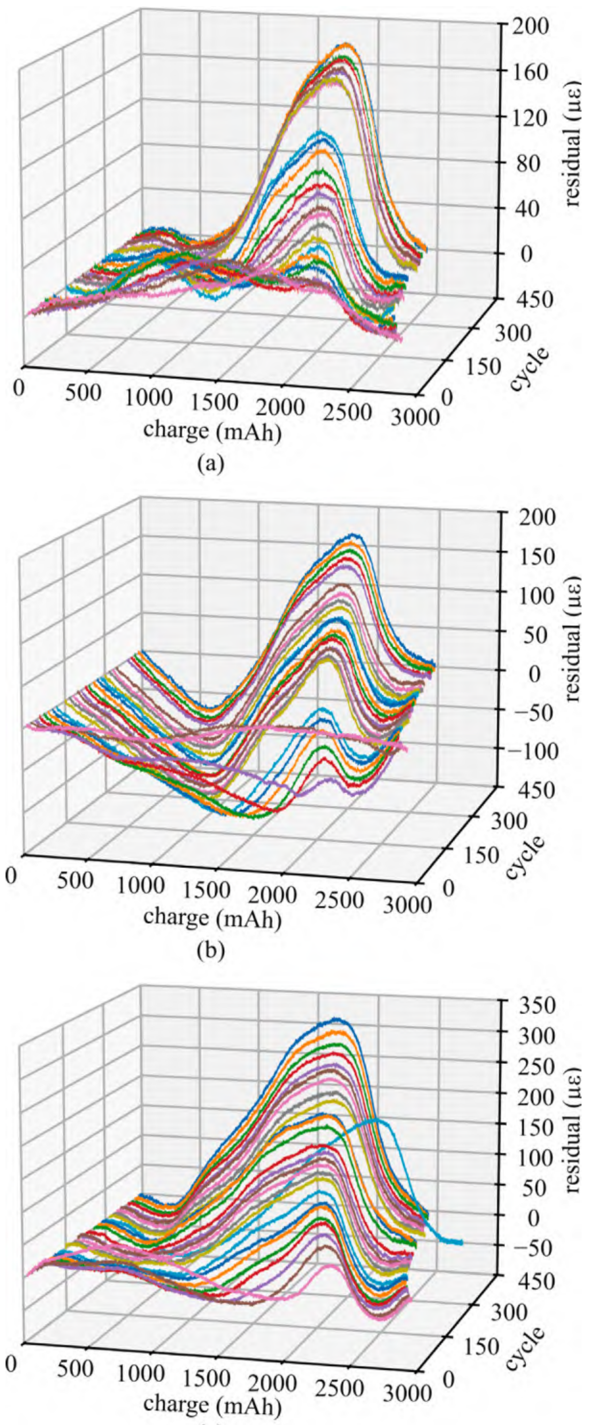

Fig. 12. Charging differential data for: (a) cell-A, (b) cell-B, and (c) cell-C.

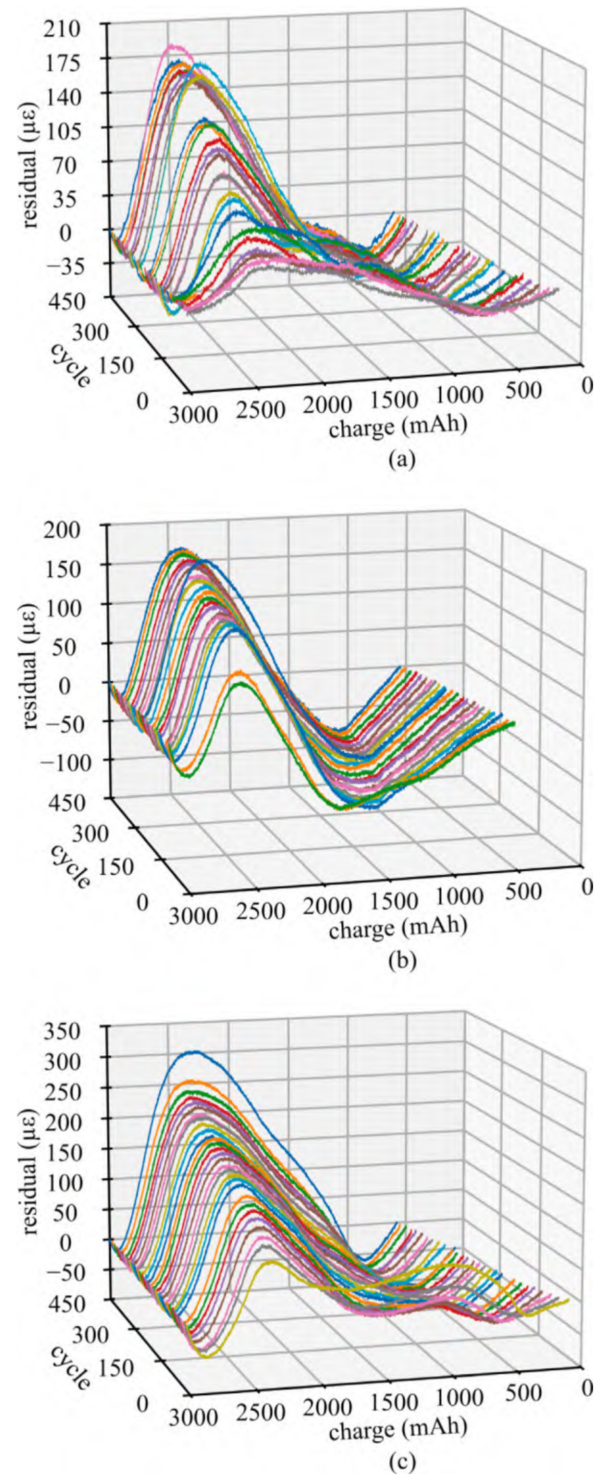

Fig. 13. Discharging differential data for: (a) cell-A, (b) cell-B, and (c) cell-C.

(b)) increase rapidly early in life and then relax toward a slower drift as aging progresses, indicating growing non-Gaussian structure; this pattern appears in both charge and discharge, with Cell-A evolving more slowly than the others. Second, the time-domain amplitude statistics (sub-figures (c) to (e)) drift gradually from early to late life, reflecting slow baseline state shifts in the strain response with low cycle-to-cycle variability. Third, the time-domain waveform ratios (sub-figures (g) to (h)) rise sharply early in life and then settle into slower evolution, with clear, localized excursions around disturbances that indicate impulsive behavior and transient peaks. These dimensionless peak-to-average measures have higher noise across cycles, making them sensitive to short, high-energy events that are muted in simple amplitude statistics, such as sub-figures (a) and (b). Lastly, the spectral localization statistics (sub-figures (i)–(j)) show a stable drift direction after the first 50 cycles. RMSF exhibits clear excursions at the overcharge events near cycles 150 and 310, whereas the frequency center remains comparatively steady and does not register these transients. This separation distinguishes experiment-dependent behavior from intrinsic system trends.

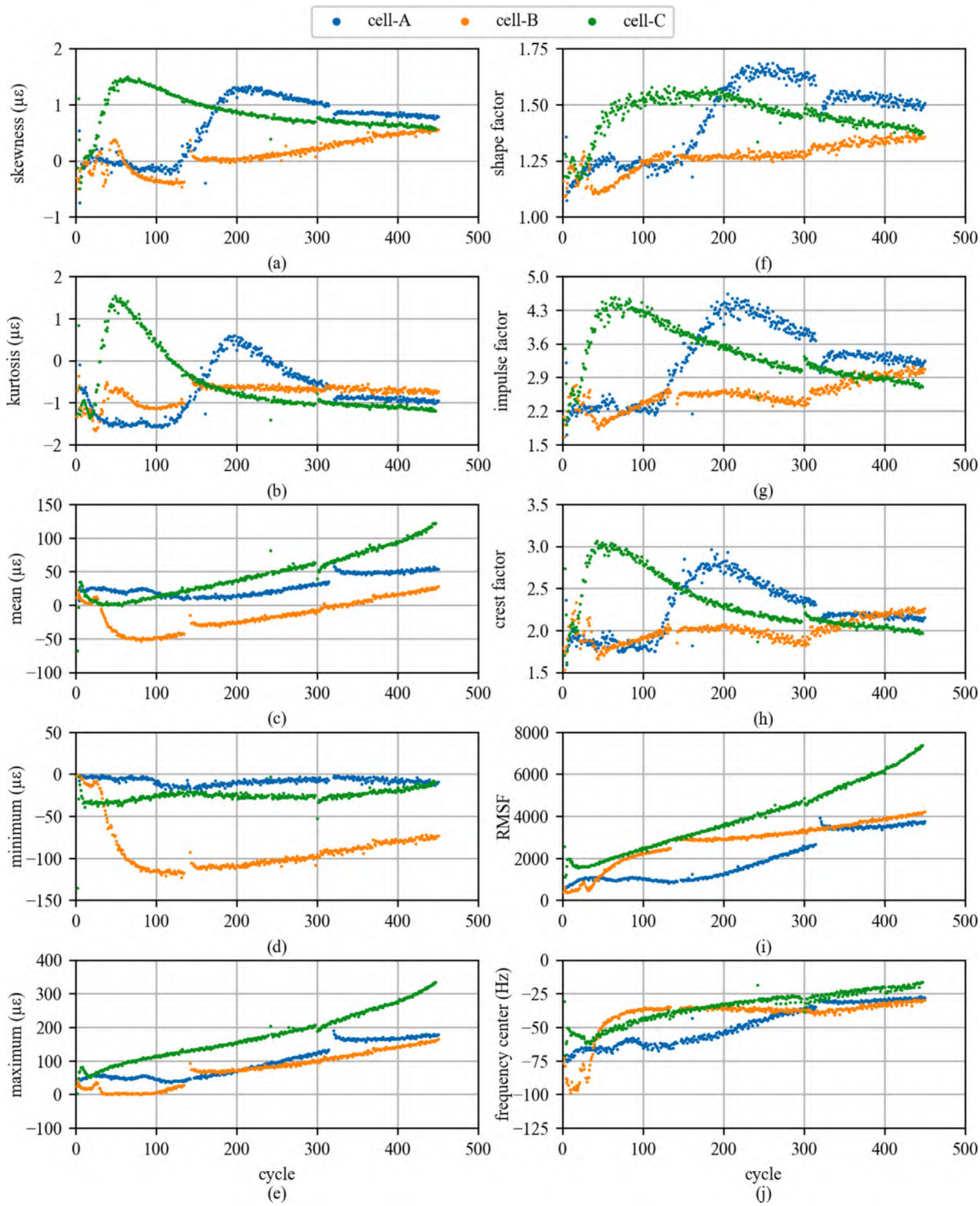

Fig. 14. Charging strain data features extracted from cell's A, B, and C.

To quantify redundancy and cross-cell consistency without crowding the main text, Table 1 reports per-feature Spearman summaries (Fisher z-averaged $\bar{\rho}$ and median $|\rho|$) for charging and discharging, with full matrices and inter-cell bar plots provided in the Appendix (Figs. 23–26). The results corroborate the patterns above, showing the features separate into two distinct behavioral groups. Maximum strain, RMSF, mean strain, and center frequency achieve high cross-cell Spearman correlations with minimal variability, indicating that these features capture degradation trends that generalize well across different cells. Conversely, crest factor, impulse factor, shape factor, and skewness display low average correlations and large spreads, suggesting that these higher-order features are highly sensitive to cell-specific effects and therefore unreliable for cross-cell SOH estimation. Intermediate features such as minimum strain and kurtosis show partial consistency but remain less stable than the amplitude-based and frequency-based metrics. Maximum strain and RMSF stand out as the most cross-cell-consistent features, exhibiting the highest average Spearman correlations and the lowest median absolute correlations in both charging and discharging.

Table 1
Cross-cell Spearman consistency per feature (charging and discharging).

Feature	Charging		Discharging	
	$\bar{\rho}$ (z-avg)	Median $\|\rho\|$	$\bar{\rho}$ (z-avg)	Median $\|\rho\|$
Mean strain	0.8406	0.1185	0.9154	0.0688
Minimum strain	0.3483	0.5669	0.5693	0.4071
Maximum strain	0.9673	0.0271	0.9585	0.0361
Crest factor	0.1822	0.6410	0.1365	0.6642
Impulse factor	0.1432	0.6931	0.1143	0.6693
Shape factor	0.3147	0.5756	0.2069	0.6366
Skewness	0.1214	0.7138	0.4645	0.5179
Kurtosis	0.3577	0.5941	0.6384	0.2990
RMSF	0.9646	0.0356	0.9566	0.0361
Frequency center	0.8141	0.1896	0.9012	0.0730

Table 2 reports across all four features with the highest Spearman correlation for cell A. The distributions reveal a consistent transition decreasing from high variable early-life and mid-life behaviors to a more stable late-life response. Maximum strain and RMSF both exhibit low early-life repeatability (coefficient of variation (CV) = 10%–15%) followed by a sharp increase in magnitude and a substantial reduction in variability as the cell ages, indicating progressive mechanical degradation. Mean strain increases slightly from early-life to mid-life, then decreases sharply in late-life and center frequency displays a less extreme version of the same pattern, ultimately aligning with the monotonic trends of the other features. Since mean strain reflects the average mechanical expansion of the cell and center frequency reflects the spectral balance of the strain waveform, their mid-life variability bumps captures the period where electrochemical behavior becomes most inconsistent, driven by heterogeneous SEI growth, evolving impedance, and the onset of material cracking. In contrast, the other features primarily describe peak expansion and high-frequency noise, which evolve more monotonically with aging and therefore do not exhibit a mid-life variability peak. While center frequency is negatively dominant during charging and positively dominant during discharging, as shown in sub-figures (j) of Figs. 14 and 15, both trends move toward a more symmetrical (near-zero) center with aging. This reflects the loss of directional waveform asymmetry as the strain response becomes increasingly chaotic and mechanically degraded. Collectively, these results demonstrate that aging manifests not only as a reduction in mechanical performance but also as a pronounced decrease in cycle-to-cycle variability with a more chaotic yet symmetrical strain waveform spectrum, providing a clear statistical signature of degradation progression. The variability data is also provided as a histogram plot in the Appendix (Fig. 27).

4.3. PCA and loading observations

Fig. 16 shows PC1–PC5 versus cycle index for charging and discharging, providing their principal component trajectories or direction of aging. Plotting PC1–PC5 against cycle was chosen because the scree and cumulative explained variance in Fig. 17 indicate that PC1+PC2+PC3+PC4+PC5 capture 99% of the cumulative explained variance for charging and discharging. PC1 carries the largest share of information with an explained variance of 48% for charging and 37% for discharging. Across all cells, PC1 evolves coherently with cycling and serves as a low-dimensional aging coordinate, with drift direction stabilizing after the initial break-in period of roughly the first 50 cycles. Cells A and C track closely in shape, with cell-B appearing as a scaled version that follows the same trend but with a different amplitude. Overcharge events near cycles 150 and 315 manifest as clear excursions in some traces, particularly in cells A and B. Cell-B exhibits a clean, orderly progression that is separated from Cells A and C, while Cells A and C follow a similar trend with different scaling.

The PCA loading patterns reveal that charging and discharging strain behavior are governed by fundamentally different combinations of mechanical and waveform-shape features. During charging, Table 3 reveals PC1 is dominated by strongly positive contributions from skewness, shape factor, impulse factor, and crest factor, indicating that the primary mode of variation arises from waveform geometry rather than strain amplitude. In contrast, Table 4 shows that the discharging PC1 is driven by large positive loadings from RMSF, maximum strain, and mean strain, while shape-based descriptors such as crest factor, kurtosis, and frequency center contribute strongly but in the opposite direction. This polarity reversal shows that high strain magnitude during discharge is associated with reductions in waveform sharpness and asymmetry. Higher-order components reinforce this distinction: charging PCs emphasize geometric descriptors, whereas discharging PCs mix amplitude-driven and spectral features. Together, these results demonstrate that charging strain evolution is shape-dominated, while discharging strain evolution is amplitude-dominated, highlighting distinct underlying physical mechanisms despite the shared feature set.

5. Conclusion

The strain decomposition method isolates the segment of strain that represents irreversible cell deformation not caused by intercalation and deintercalation. The captured data is associated with internal electrochemical reactions and enables the systematic observation of cell aging. Cycle-to-cycle correlation analysis reveals that as the cell ages, mechanical capability declines while the strain waveform progressively converges toward stable, symmetric spectral patterns, providing a clear statistical trajectory of advanced degradation. PCA is employed to reduce the dimensionality of both charging and discharging feature spaces by 50% while preserving the majority of relevant variance. Notably, the retention of the first five principal components for charging and discharging accounts for approximately 99% of the total variance. This dimensionality reduction supports efficient monitoring of degradation patterns and minimizes the confounding effects of noise. PCA loading analysis suggests that charging PC1 increases when waveform-shape features increase. During discharging, high strain magnitude is associated with lower waveform-shape metrics. Consequently, this targeted approach facilitates clearer visualization and analysis of aging trajectories, thereby providing a robust framework for identifying dominant strain modes and their evolution throughout electrochemical cycling. While the methodology introduced in this paper focused exclusively on individual cylindrical 18650 NMC cells, the method could potentially be expanded to different cell geometries, sizes, and module-level conditions. Since various cell geometries and modular cell interactions would affect strain signatures significantly, such expansion would require a multitude of dedicated experiments outside the scope of this paper. Future work will focus on this generalization strain degradation problem to progress this work further.

Abbreviations

The following abbreviations are used in this manuscript:
SOH: State-of-Health
IOECM: Integer-Order Equivalent Circuit Model
FOECM: Fractional-Order Equivalent Circuit Model
BMS: Battery Management System
SOC: State-of-Charge
FBG: Fiber Bragg Grating
DIC: Digital Image Correlation
XRD: X-ray Diffraction
SEI: Solid Electrolyte Interphase
CID: Current Interrupt Device
CCCV: Constant Current–Constant Voltage
CC: Constant Current
CV: Constant Voltage
MAE: Mean Absolute Error
RMSE: Root Mean Square Error
RMSF: Root Mean Square Frequency
PC: Principal Component

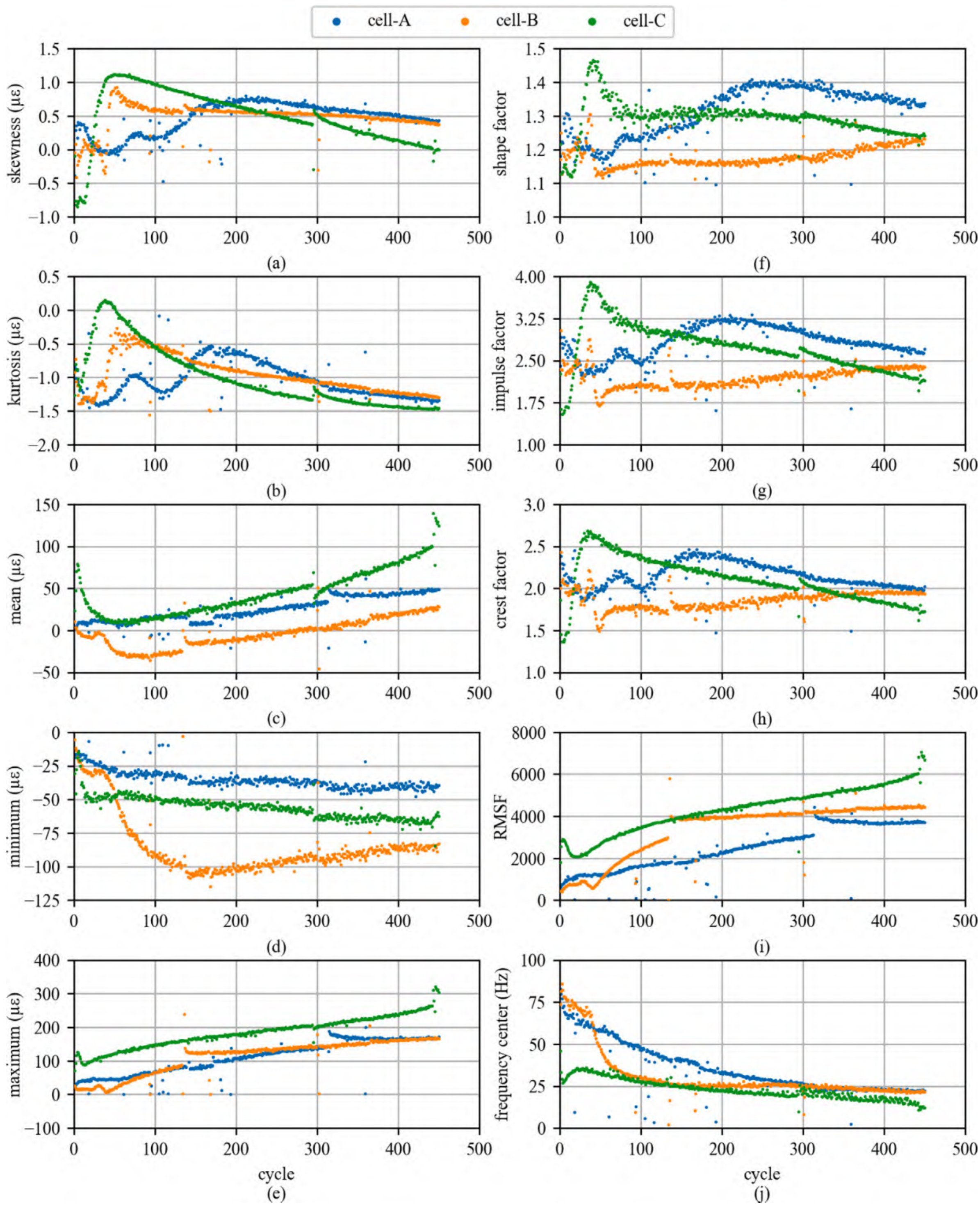

Fig. 15. Discharging strain data features extracted from cell's A, B, and C.

Table 2
Early-life, mid-life, and late-life variability statistics for maximum strain, RMSF, mean strain, and center frequency.

Feature	Early-life			Mid-life			Late-life		
	mean	std	CV	mean	std	CV	mean	std	CV
Max strain	52.27	5.17	0.098	85.44	7.81	0.0914 9	172.64	4.06	0.0235
Mean strain	23.06	3.02	0.1308	17.91	2.68	0.1496	52.11	2.28	0.0437
RMSF	955.83	141.25	0.1478	1619.93	173.20	0.1069	3625.45	80.12	0.0221
Center frequency	−67.64	2.82	−0.0417	−47.96	3.10	−0.0647	−28.95	0.86	−0.0297

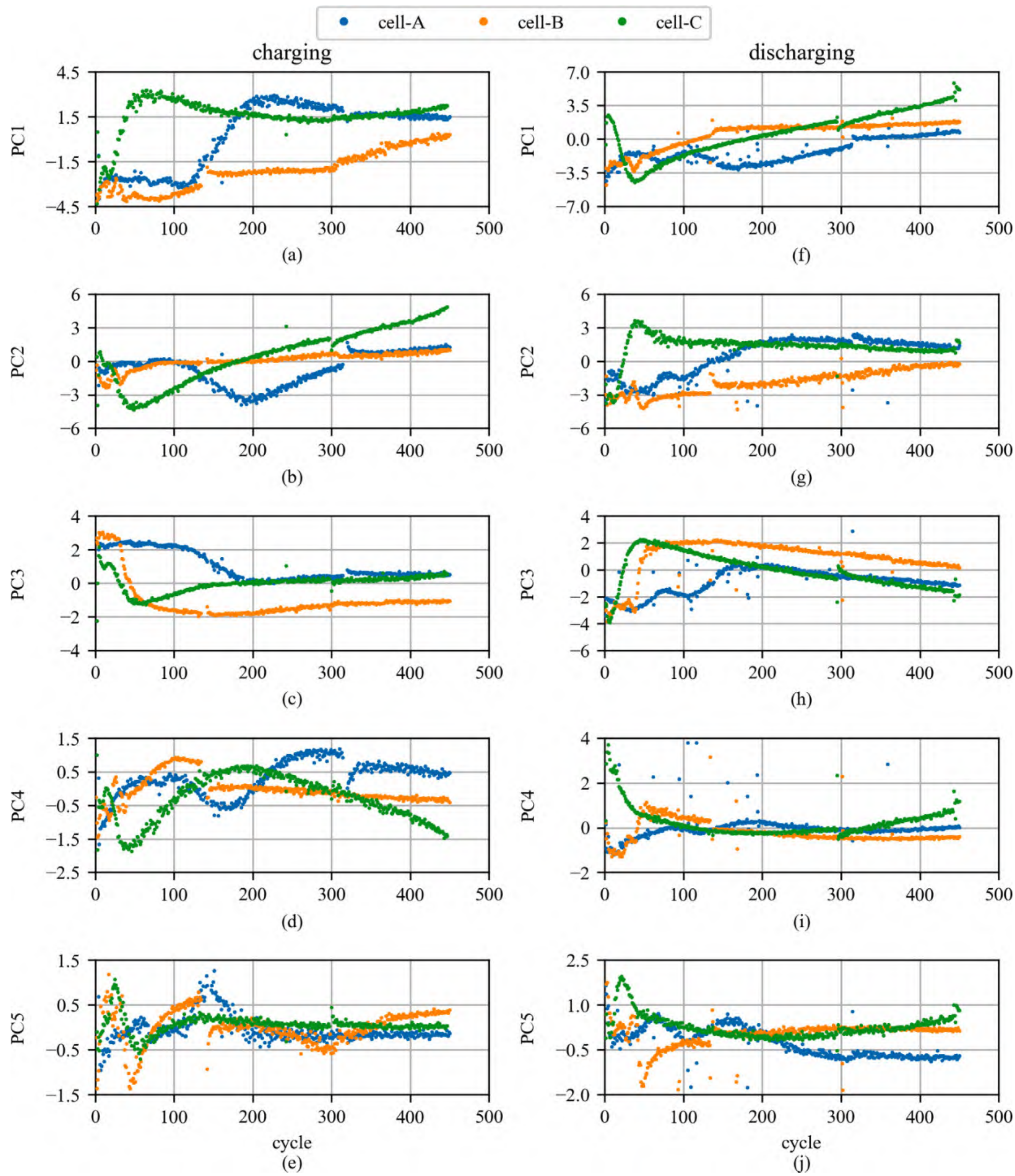

Fig. 16. PC1–PC5 versus cycles from cell's A, B, and C for charging and discharging.

Table 3
PCA feature loadings for the principal components (charging).

Feature	PC1	PC2	PC3	PC4	PC5	PC6	PC7	PC8	PC9	PC10
RMSF	0.4391	0.8279	−0.3020	−0.1520	0.0438	−0.0633	0.0048	0.0456	−0.0142	−0.0049
Maximum strain	0.6716	0.7190	0.0046	−0.1732	0.0087	−0.0412	0.0022	−0.0083	0.0297	0.0083
Mean strain	0.6526	0.5794	0.4586	−0.1591	0.0001	0.0003	−0.0372	−0.0435	−0.0185	−0.0033
Crest factor	0.7136	−0.6416	−0.1114	−0.1486	0.2049	0.0567	0.0048	−0.0031	0.0076	−0.0101
Shape factor	0.9151	−0.0577	−0.0139	0.3835	−0.0269	−0.0984	−0.0477	−0.0037	0.0066	−0.0092
Minimum strain	0.5586	−0.0712	0.8191	0.0131	−0.0573	0.0851	−0.0236	0.0387	0.0046	−0.0004
Kurtosis	0.4869	−0.7008	−0.4038	−0.2727	−0.1714	−0.0016	−0.0759	0.0021	0.0002	−0.0014
Frequency center	0.4450	0.6790	−0.5299	0.1831	−0.0298	0.1617	−0.0210	−0.0051	−0.0004	0.0003
Impulse factor	0.8735	−0.4622	−0.0737	0.0970	0.0885	−0.0176	−0.0267	0.0053	−0.0132	0.0183
Skewness	0.9526	−0.2428	−0.0402	0.0014	−0.1001	0.0016	0.1509	−0.0058	−0.0043	−0.0009

Table 4
PCA feature loadings for the principal components (discharging).

Feature	PC1	PC2	PC3	PC4	PC5	PC6	PC7	PC8	PC9	PC10
RMSF	0.8528	0.4373	0.2193	−0.1000	0.1292	0.0641	0.0102	−0.0541	−0.0204	−0.0017
Maximum strain	0.7483	0.6471	0.0492	−0.0135	0.1043	0.0850	−0.0072	−0.0239	0.0260	0.0026
Mean strain	0.5105	0.6468	−0.5125	0.1832	0.0824	0.1177	−0.0113	0.0694	−0.0075	−0.0010
Crest factor	−0.6640	0.6820	0.0576	−0.0961	0.2333	−0.1152	−0.1200	0.0052	0.0022	−0.0097
Shape factor	−0.2758	0.9061	−0.1522	−0.0503	−0.1841	−0.0350	0.2067	−0.0065	0.0014	−0.0065
Minimum strain	−0.5946	0.3275	−0.6787	0.1651	−0.1584	0.1028	−0.1167	−0.0534	−0.0015	0.0002
Kurtosis	−0.6394	−0.0061	0.6357	0.3837	0.1625	0.0880	0.0784	−0.0133	−0.0001	−0.0007
Frequency center	−0.6779	−0.4571	−0.4194	−0.2610	0.2013	0.2024	0.0823	−0.0001	0.0012	0.0000
Impulse factor	−0.5703	0.8101	−0.0016	−0.0658	0.0815	−0.0870	0.0182	0.0034	−0.0052	0.0150
Skewness	−0.3225	0.4393	0.7696	−0.1652	−0.2066	0.1844	−0.0829	0.0253	−0.0013	−0.0001

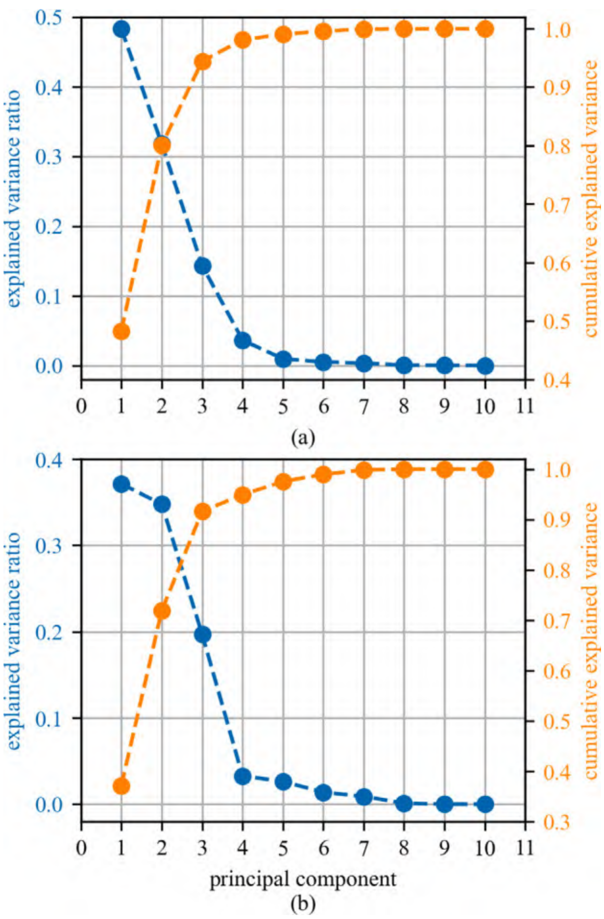

Fig. 17. Scree plot of the principal components and cumulative explained variance plot for: (a) charging and (b) discharging features.

CRediT authorship contribution statement

Malichi Flemming: Writing – review & editing, Writing – original draft, Visualization, Validation, Methodology, Investigation, Formal analysis, Data curation. **George Anthony:** Writing – original draft, Methodology, Data curation, Conceptualization. **Ryan L. Limbaugh:** Writing – original draft, Visualization, Methodology, Conceptualization. **Austin R.J. Downey:** Writing – review & editing, Supervision, Resources, Project administration, Investigation, Conceptualization.

Declaration of competing interest

The authors declare the following financial interests/personal relationships which may be considered as potential competing interests: Austin Downey reports financial support was provided by National Science Foundation. If there are other authors, they declare that they have no known competing financial interests or personal relationships that could have appeared to influence the work reported in this paper.

Acknowledgments

This work is supported by the National Science Foundation (NSF) grant number CPS - 2237696. Additionally, this work was supported, in part, at The University of South Carolina by the State of South Carolina through funding for the Battelle Savannah River Alliance Workforce Development Program. Any opinions, findings, conclusions, or recommendations expressed in this material are those of the authors and do not necessarily reflect the views of the National Science Foundation.

Appendix 6

This Appendix compiles supplementary materials that support, but are not essential to, the main narrative. Here the complete cycle-wise strain for all cells are presented. Furthermore, Cycle–100 charge/discharge snapshots for Cells B and C and the full Spearman correlation analyses for charging and discharging (matrices and inter-cell summaries) are provided for completeness and reproducibility.

6.1. 3D charge–discharge cycles

Fig. 18 shows 3D subplots of strain as a function of time (x-axis) and cycle number (y-axis) for cells A, B, and C. The left column displays charging traces and the right column discharging traces.

6.2. Charge cycle

Figs. 19–22 show cycle 100's charge and discharge data for cells B and C. The charge and discharge data at cycle 100 for cell-A was shown in Fig. 7.

6.3. Spearman correlations

Figs. 23–26 report Spearman rank correlations for both charging and discharging. The matrices (Figs. 23 and 24) summarize within-cell associations among features with per-feature scores, while the bar plots (Figs. 25 and 26) aggregate inter-cell agreement to assess consistency across Cells A–C.

6.4. Cell a variability

Fig. 27 reports distributional evolution of four mechanical features across early-life, mid-life, and late-life cycling for cell A. Histograms illustrate how the underlying distributions shift and widen as the cell ages. Early-life cycles exhibit loose, unstable distributions, whereas mid-life and late-life cycles show substantial reductions in central tendency and increased variability.

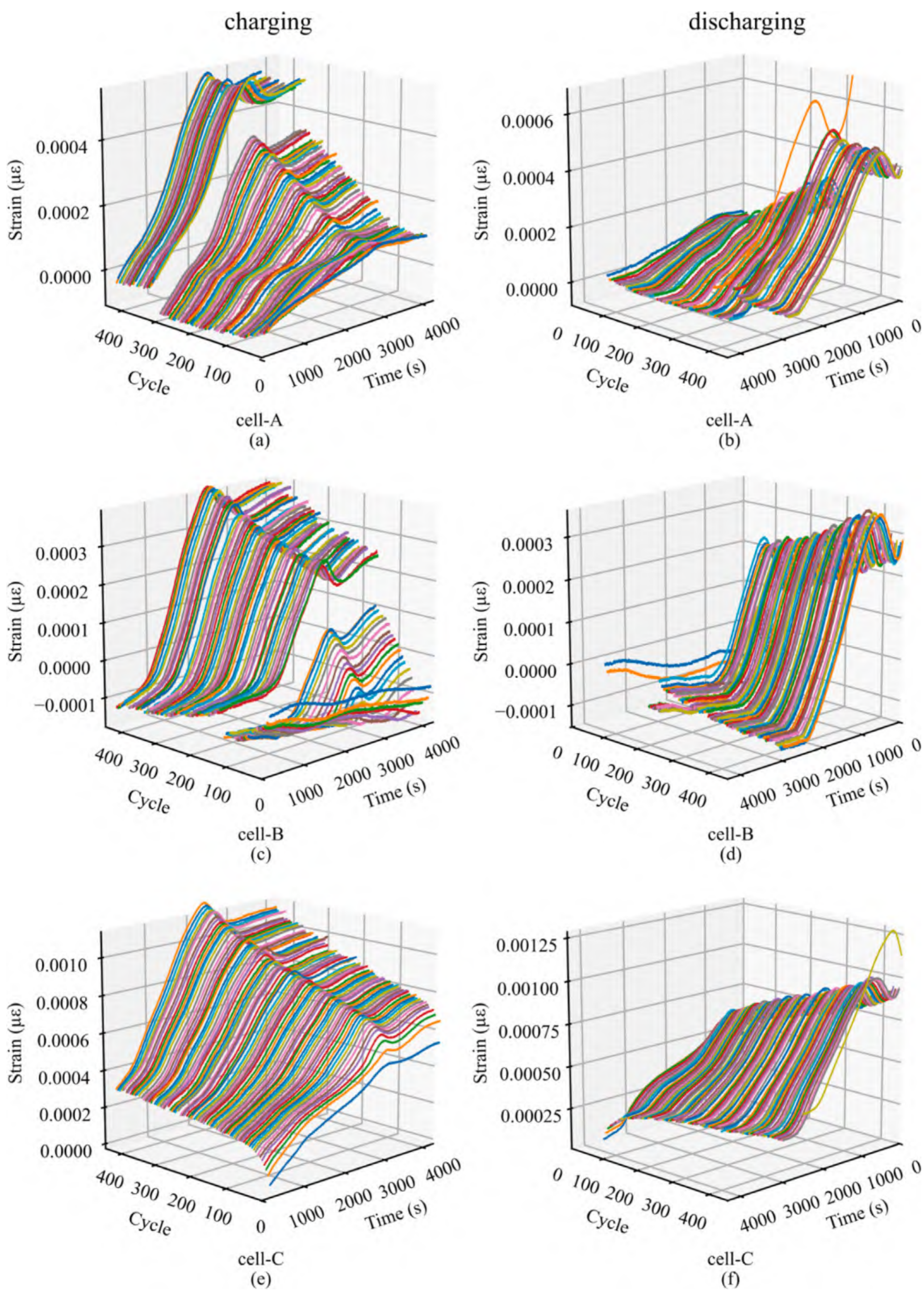

Fig. 18. Charging and discharging cycle-wise strain for cells A, B, and C.

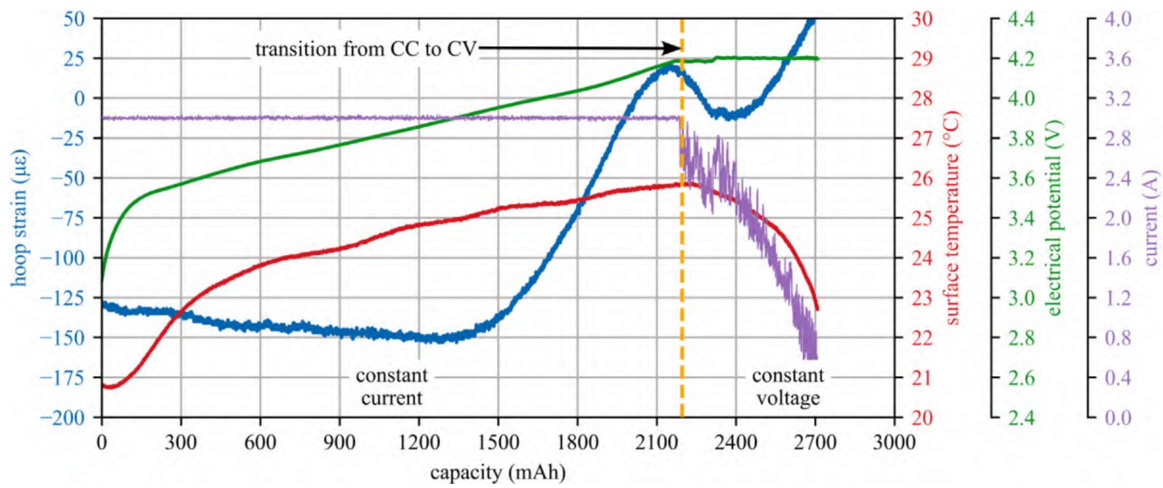

Fig. 19. Cycle 100 charge data for cell-B.

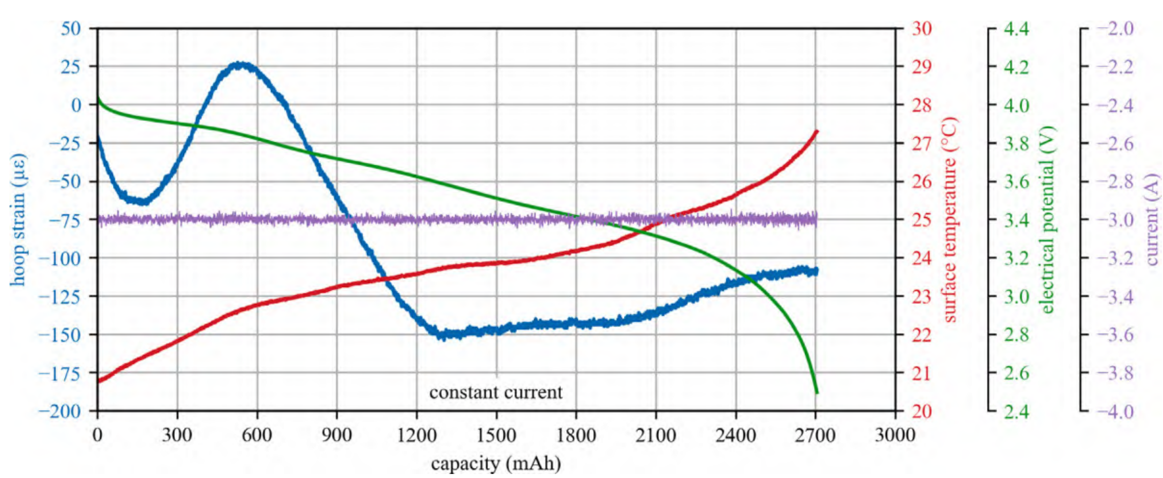

Fig. 20. Cycle 100 discharge data for cell-B.

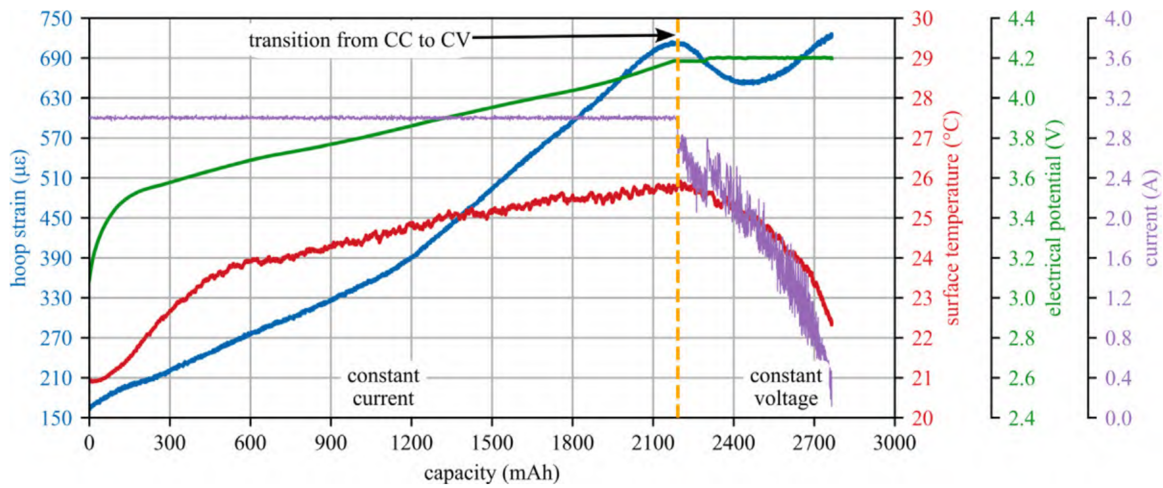

Fig. 21. Cycle 100 charge data for cell-C.

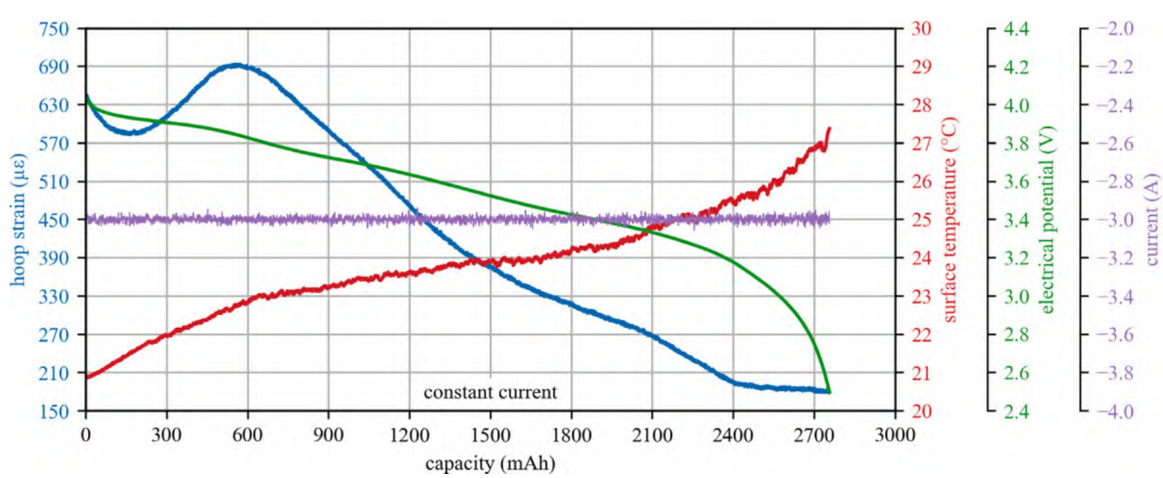

Fig. 22. Cycle 100 discharge data for cell-C.

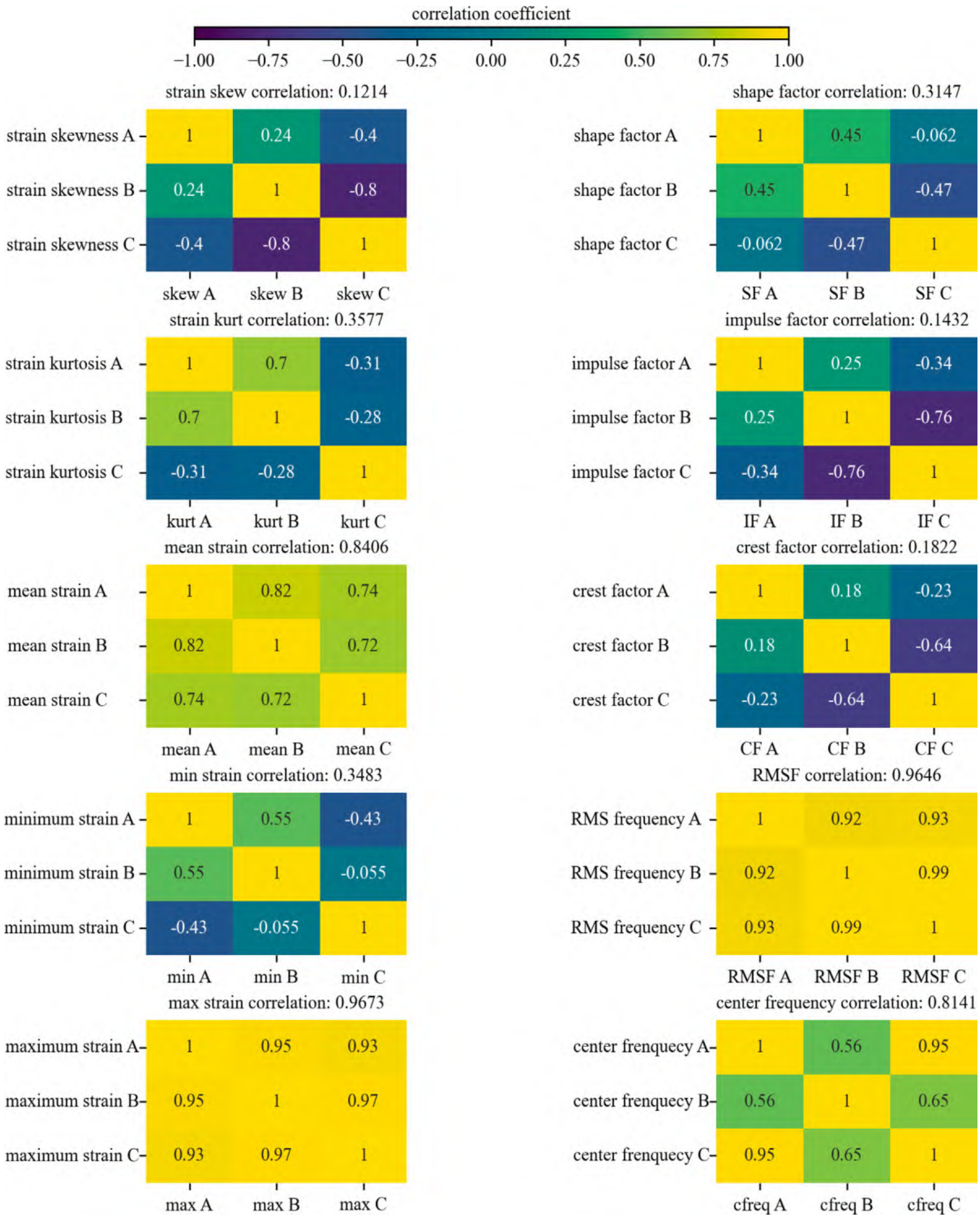

Fig. 23. Charging Spearman correlation matrix and score for each feature extracted from cell's A, B, and C.

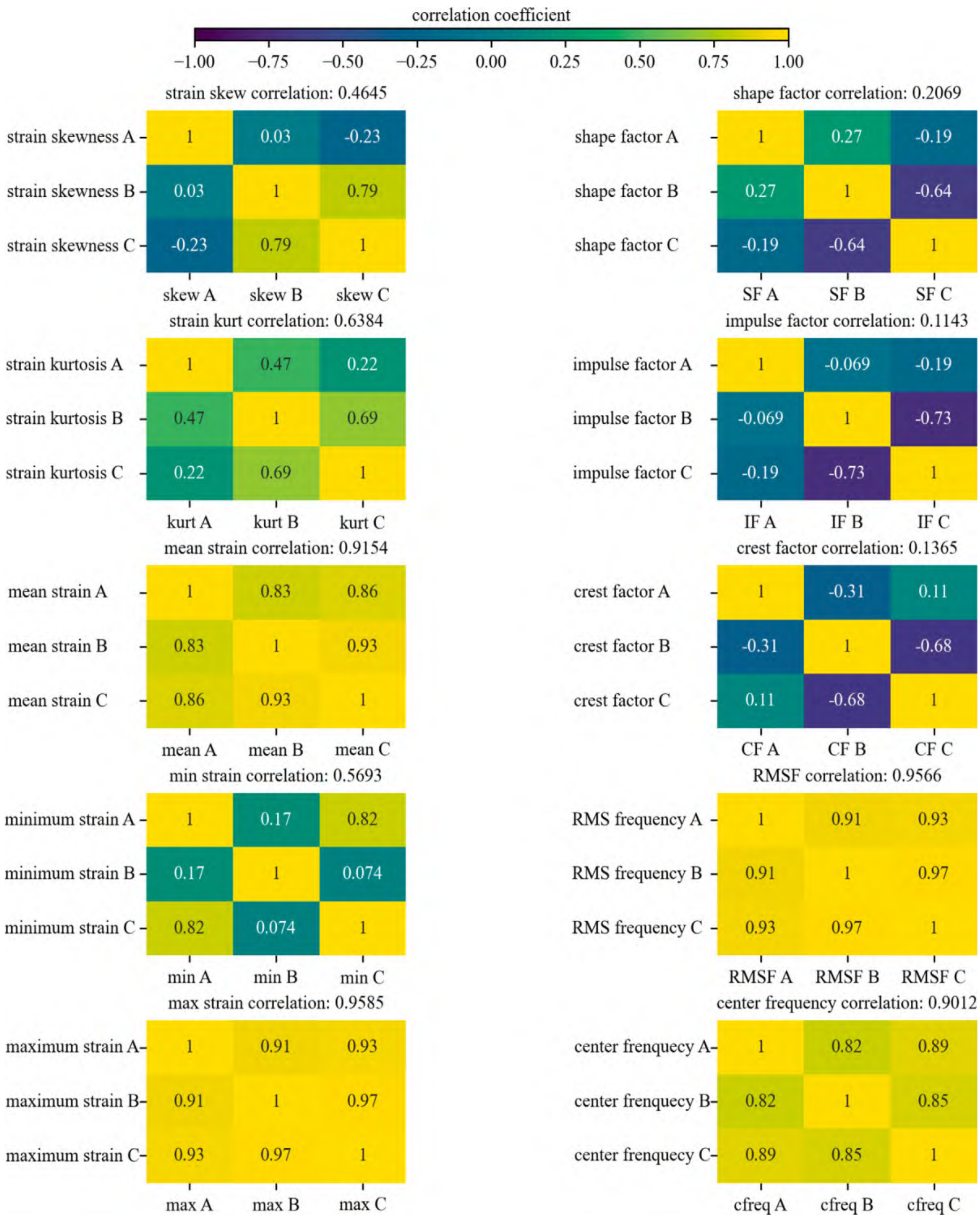

Fig. 24. Discharging Spearman correlation matrix and score for each feature extracted from cell's A, B, and C.

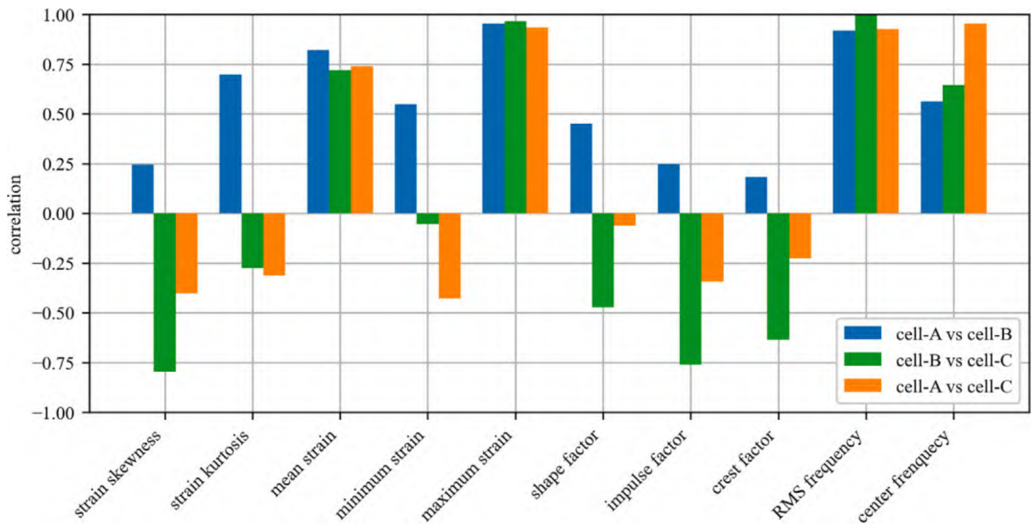

Fig. 25. Charging bar plot representing Spearman correlations between cells.

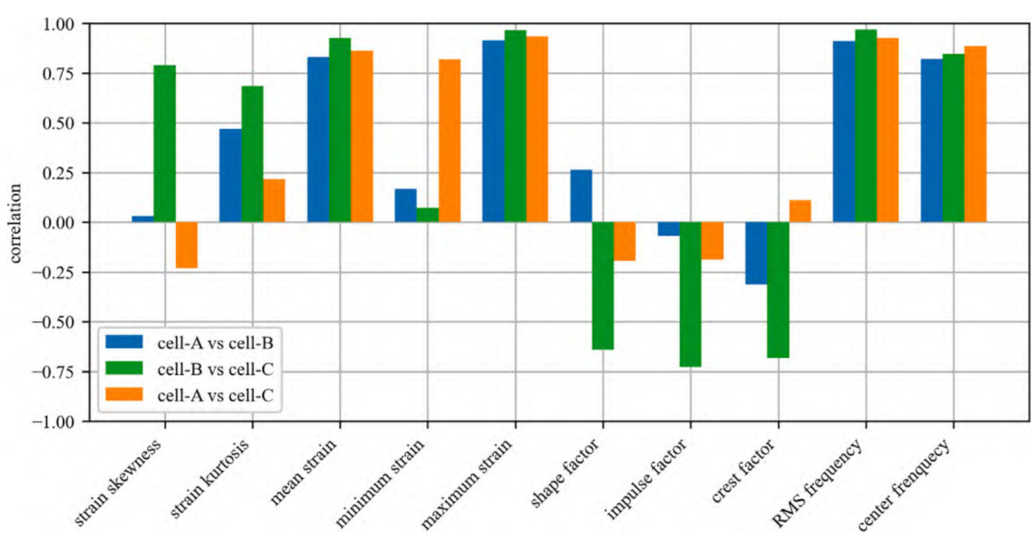

Fig. 26. Discharging bar plot representing Spearman correlations between cells.

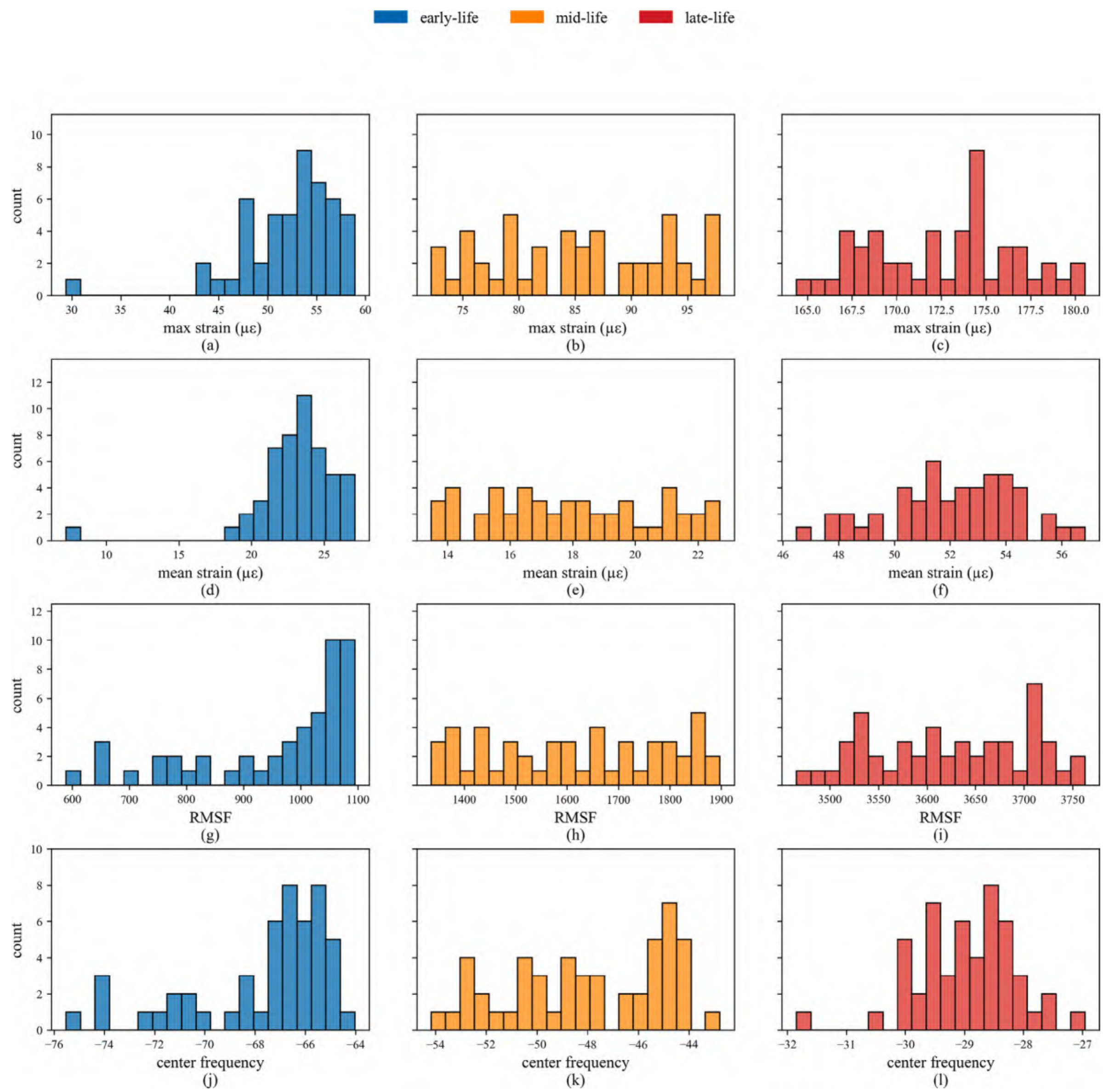

Fig. 27. Early-life, mid-life, and late-life variability statistics for maximum strain, RMSF, mean strain, and center frequency.

Data availability

Data used in this work is available through a public repository.

Dataset-1 (Original data) (dataset-cycling-with-strain-monitoring-for-samsung-30Q-cell).

References

[1] Pooya Parvizi, Milad Jalilian, Alireza Mohammadi Amidi, Mohammad Reza Zangeneh, Jordi-Roger Riba, From present innovations to future potential: The promising journey of lithium-ion batteries, Micromachines 16 (2) (2025) 194.

[2] Lingzhi Su, Yan Xu, Zhaoyang Dong, State-of-health estimation of lithium-ion batteries: A comprehensive literature review from cell to pack levels, Energy Convers. Econ. 5 (4) (2024) 224–242.

[3] Alvin J Salkind, Craig Fennie, Pritpal Singh, Terrill Atwater, David E Reisner, Determination of state-of-charge and state-of-health of batteries by fuzzy logic methodology, J. Power Sources 80 (1–2) (1999) 293–300.

[4] Cezar Comanescu, Ensuring safety and reliability: An overview of lithium-ion battery service assessment, Batteries 11 (1) (2024) 6.

[5] Idris T. Adebanjo, Juliana Eko, Anita G. Agbeyegbe, Simuck F. Yuk, Samuel V. Cowart, Enoch A. Nagelli, F. John Burpo, Jan L. Allen, Dat T. Tran, Nishma Bhattarai, Krishna Shah, Jang-Yeon Hwang, H. Hohyun Sun, A comprehensive review of lithium-ion battery components degradation and operational considerations: a safety perspective, Energy Adv. 4 (7) (2025) 820–877.

[6] Nicola Campagna, Vincenzo Castiglia, Rosario Miceli, Rosa Anna Mastromauro, Ciro Spataro, Marco Trapanese, Fabio Viola, Battery models for battery powered applications: A comparative study, Energies 13 (16) (2020) 4085.

[7] Lijun Zhang, Hui Peng, Zhansheng Ning, Zhongqiang Mu, Changyan Sun, Comparative research on RC equivalent circuit models for lithium-ion batteries of electric vehicles, Appl. Sci. 7 (10) (2017) 1002.

[8] Pablo Rodríguez-Iturriaga, David Anseán, Salvador Rodríguez-Bolívar, Manuela González, Juan Carlos Viera, Juan Antonio López-Villanueva, A physics-based fractional-order equivalent circuit model for time and frequency-domain applications in lithium-ion batteries, J. Energy Storage 64 (2023) 107150.

[9] Xinyuan Wei, Longxing Wu, Chunhui Liu, Zhiyuan Si, Xing Shu, Heng Li, Comparative evaluation of fractional-order models for lithium-ion batteries response to novel drive cycle dataset, Fractal Fract. 9 (7) (2025) 429.

[10] Austin Downey, Yu-Hui Lui, Chao Hu, Simon Laflamme, Shan Hu, Physics-based prognostics of lithium-ion battery using non-linear least squares with dynamic bounds, Reliab. Eng. Syst. Saf. 182 (2019) 1–12.

[11] Babatunde D. Soyoye, Indranil Bhattacharya, Mary Vinolisha Anthony Dhason, Trapa Banik, State of charge and state of health estimation in electric vehicles: Challenges, approaches and future directions, Batteries 11 (1) (2025) 32.

[12] Christopher Hendricks, Bhanu Sood, Michael Pecht, Lithium-ion battery strain gauge monitoring and depth of discharge estimation, J. Electrochem. Energy Convers. Storage 20 (1) (2022).

[13] Xiaoran Hu, Zhaolian Jiang, Liqin Yan, Guiting Yang, Jingying Xie, Shuai Liu, Qian Zhang, Yong Xiang, Hang Min, Xiaoli Peng, Real-time visualized battery health monitoring sensor with piezoelectric/pyroelectric poly (vinylidene fluoride-trifluoroethylene) and thin film transistor array by in-situ poling, J. Power Sources 467 (2020) 228367.

[14] Bruno Rente, Matthias Fabian, Miodrag Vidakovic, Xuan Liu, Xiang Li, Kang Li, Tong Sun, Kenneth T.V. Grattan, Lithium-ion battery state-of-charge estimator based on FBG-based strain sensor and employing machine learning, IEEE Sensors J. 21 (2) (2021) 1453–1460.

[15] Goerge Anthony, Connor Madden, Emmanuel Ogunniyi, Austin R.J. Downey, Ryan Limbaugh, Jarret Peskar, Jingjing Bao, Xinyu Huang, Exploratory investigation of early detection for high-C discharge-induced failure in 18650 lithium-ion batteries, in: Zhongqing Su, Kara J. Peters, Fabrizio Ricci, Piervincenzo Rizzo (Eds.), Health Monitoring of Structural and Biological Systems XVIII, Vol. 12951, SPIE International Society for Optics and Photonics, 2024, 129510Q.

[16] B. Koohbor, L. Sang, Ö.Ö. Çapraz, A.A. Gewirth, R.G. Nuzzo, S.R. White, N.R. Sottos, In situ strain measurement in solid-state li-ion batteries, in: Fracture, Fatigue, Failure and Damage Evolution, Volume 6, River Publishers, 2025, pp. 1–3.

[17] Natalia Andrea Cañas, Philipp Einsiedel, Oliver Thomas Freitag, Christopher Heim, Miriam Steinhauer, Dong-Won Park, Kaspar Andreas Friedrich, Operando X-ray diffraction during battery cycling at elevated temperatures: A quantitative analysis of lithium-graphite intercalation compounds, Carbon 116 (2017) 255–263.

[18] Edris Akbari, George Z. Voyiadjis, Stress and strain characterization for evaluating mechanical safety of lithium-ion pouch batteries under static and dynamic loadings, Batteries 10 (9) (2024) 309.

[19] Wenju Ren, Taixiong Zheng, Changhao Piao, Daryn Eugene Benson, Xin Wang, Haiqing Li, Shen Lu, Characterization of commercial 18650 li-ion batteries using strain gauges, J. Mater. Sci. 57 (28) (2022) 13560–13569.

[20] Connor Madden, Austin R.J. Downey, Austin R.J. Downey, Yohanna MejiaCruz, Robin James, Inferring battery current interrupt device activation in a 18650 cell under high c discharge using a foil strain gauge, in: ASNT Research Symposium 2024 Proceedings, The American Society for Nondestructive Testing, 2024.

[21] Malichi Flemming, George Anthony, Ryan Limbaugh, Austin R. Downey, Exploratory analysis of strain-derived features for machine-learning estimation of state of health in 18 650 lithium-ion cells.

[22] George Anthony, Malichi Flemming, Andrew Weng, Austin R. Downey, Ralph White, Kerry Sado, Strain-based investigation of current imbalance and lithium intercalation stages in parallel-connected lithium-ion cells.

[23] Jun Peng, Shuhai Jia, Shuming Yang, Xilong Kang, Hongqiang Yu, Yaowen Yang, State estimation of lithium-ion batteries based on strain parameter monitored by fiber bragg grating sensors, J. Energy Storage 52 (2022) 104950.

[24] Xiaolei Bian, Changfu Zou, Björn Fridholm, Christian Sundvall, Torsten Wik, Smart sensing breaks the accuracy barrier in battery state monitoring, Energy Storage Mater. 80 (2025) 104410.

[25] Yihuan Li, Kang Li, Xuan Liu, Xiang Li, Li Zhang, Bruno Rente, Tong Sun, Kenneth T.V. Grattan, A hybrid machine learning framework for joint SOC and SOH estimation of lithium-ion batteries assisted with fiber sensor measurements, Appl. Energy 325 (2022) 119787.

[26] Bernhard Bitzer, Andreas Gruhle, A new method for detecting lithium plating by measuring the cell thickness, J. Power Sources 262 (2014) 297–302.

[27] Shengxin Zhu, Le Yang, Jinbao Fan, Jiawei Wen, Xiaolong Feng, Peijun Zhou, Fuguo Xie, Jiang Zhou, Ya-Na Wang, In-situ obtained internal strain and pressure of the cylindrical li-ion battery cell with silicon-graphite negative electrodes, J. Energy Storage 42 (2021) 103049.

[28] Lei Tao, Dawei Xia, Poom Sittisomwong, Hanrui Zhang, Jianwei Lai, Sooyeon Hwang, Tianyi Li, Bingyuan Ma, Anyang Hu, Jungki Min, Dong Hou, Sameep Rajubhai Shah, Kejie Zhao, Guang Yang, Hua Zhou, Luxi Li, Peng Bai, Feifei Shi, Feng Lin, Solvent-mediated, reversible ternary graphite intercalation compounds for extreme-condition li-ion batteries, J. Am. Chem. Soc. 146 (24) (2024) 16764–16774.

[29] Bin Wang, Lewis W. Le Fevre, Adam Brookfield, Eric J.L. McInnes, Robert A.W. Dryfe, Resolution of lithium deposition versus intercalation of graphite anodes in lithium ion batteries: An in situ electron paramagnetic resonance study, Angew. Chem. Int. Ed. 60 (40) (2021) 21860–21867.

[30] Aiping Wang, Sanket Kadam, Hong Li, Siqi Shi, Yue Qi, Review on modeling of the anode solid electrolyte interphase (SEI) for lithium-ion batteries, Npj Comput. Mater. 4 (1) (2018).

[31] Borong Li, Yu Chao, Mengchao Li, Yuanbin Xiao, Rui Li, Kang Yang, Xiancai Cui, Gui Xu, Lingyun Li, Chengkai Yang, Yan Yu, David P. Wilkinson, Jiujun Zhang, A review of solid electrolyte interphase (SEI) and dendrite formation in lithium batteries, Electrochem. Energy Rev. 6 (1) (2023).

[32] Jun Ma, Cody Gonzalez, Qingquan Huang, Joseph Farese, Christopher Rahn, Mary Frecker, Donghai Wang, Multifunctional Li(Ni0.5Co0.2Mn0.3) O2-Si batteries with self-actuation and self-sensing, J. Intell. Mater. Syst. Struct. 31 (6) (2020) 860–868.

[33] Sourav Das, Pranav Shrotriya, Electrochemical mechanism underlying lithium plating in batteries: Non-invasive detection and mitigation, Energies 17 (23) (2024) 5930.

[34] Angel Kirchev, Nicolas Guillet, Loic Lonardoni, Sebastien Dumenil, Li-ion cell safety monitoring using mechanical parameters, part 3: Battery behaviour during abusive overcharge, Batteries 9 (7) (2023).

[35] Vishay Precision Group, Micro-Measurements, M-bond 200 adhesive data sheet, 2023, Document No. 11031.

[36] Vishay Precision Group, Micro-Measurements, Strain gage installation accessories, 2023, Catalog 11029.

[37] ARTS-Lab, Dataset cycling with strain monitoring for samsung 30Q Cell https://github.com/ARTS-Laboratory/dataset-cycling-with-strain-monitoring-for-samsung-30Q-cell GitHub.